ULPGC Universidad de Las Palmas de Gran Canaria | Instituto Universitario de Microelectrónica Aplicada IUMA

Mater of Science in Applied Electronics and Telecommunications (META)

Master's Thesis

Stitching Algorithms for Automatic Assembly of Hyperspectral Histological Images

Author: Laura Quintana Quintana
Supervisor(s): Gustavo Marrero Callicó
Samuel Ortega Sarmiento
Himar Fabelo Gómez

Date: July 2020

IUMA
t +34 928 451 150
+34 928 451 086
f +34 928 451 083
e: iuma@iuma.ulpgc.es
w: www.iuma.ulpgc.es
Campus Universitario de Tafira
35017 Las Palmas de Gran Canaria

ULPGC Universidad de Las Palmas de Gran Canaria | Instituto Universitario de Microelectrónica Aplicada IUMA

Mater of Science in Applied Electronics and Telecommunications (META)

IUMA

Master's Thesis

Stitching Algorithms for Automatic Assembly of Hyperspectral Histological Images

HOJA DE FIRMAS

Author:	Laura Quintana Quintana	Signature:	QUINTANA QUINTANA LAURA - 45332725R Firmado digitalmente por QUINTANA QUINTANA LAURA - 45332725R Fecha: 2020.07.20 18:51:27 Z
Supervisor:	Gustavo Marrero Callicó	Signature:	MARRERO CALLICO GUSTAVO - 42875067P Firmado digitalmente por MARRERO CALLICO GUSTAVO - 42875067P Fecha: 2020.07.21 12:17:26 +01'00'
Supervisor:	Samuel Ortega Sarmiento	Signature:	ORTEGA SARMIENTO SAMUEL - 78524517X Firmado digitalmente por ORTEGA SARMIENTO SAMUEL - 78524517X Fecha: 2020.07.21 15:43:18 +01'00'
Supervisor:	Himar Fabelo Gómez	Signature:	FABELO GOMEZ HIMAR ANTONIO - 78528094E Firmado digitalmente por FABELO GOMEZ HIMAR ANTONIO - 78528094E Nombre de reconocimiento (DN): c=ES, serialNumber=IDCES-78528094E, givenName=HIMAR ANTONIO, sn=FABELO GOMEZ, cn=FABELO GOMEZ HIMAR ANTONIO - 78528094E Fecha: 2020.07.21 11:58:47 +01'00'
Date:	**July 2020**		

IUMA
t +34 928 451 150
+34 928 451 086
f +34 928 451 083
e: iuma@iuma.ulpgc.es
w: www.iuma.ulpgc.es
Campus Universitario de Tafira
35017 Las Palmas de Gran Canaria

ULPGC Universidad de Las Palmas de Gran Canaria | Instituto Universitario de Microelectrónica Aplicada IUMA

Mater of Science in Applied Electronics and Telecommunications (META)

Master's Thesis

Stitching Algorithms for Automatic Assembly of Hyperspectral Histological Images

EVALUATION

Calification: .....

President Signature:

Secretary Signature:

Member Signature:

Date: July 2020

IUMA
t +34 928 451 150
+34 928 451 086
f +34 928 451 083
e: iuma@iuma.ulpgc.es
w: www.iuma.ulpgc.es
Campus Universitario de Tafira
35017 Las Palmas de Gran Canaria

Abstract

Nowadays, the study of histology slides is considered the gold standard for the clinical diagnosis of cancer, and current trend is to digitalize histology slides for further histology image analysis. Histopathologists visually examine the regularities of cell shapes and tissue distributions, decide whether tissue regions are cancerous, and determine the malignancy level. However, the interpretation of these images is often subjective due to limitations in human vision to distinguish subtle color differences particularly because of spatially overlapping emissions.

Spectral technology improves on color camera performance by expanding the number of channels beyond the RGB palette. The higher content of information (spatial and spectral) provided by a hyperspectral image of a scene can be analyzed to detect, identify, or discriminate objects and patterns as well as the chemical composition of the material present at the scene. However, spatial information provided by a hyperspectral (HS) or multispectral (MS) frame is usually lower compared to a traditional RGB frame. Microimage stitching offers an approach for expansion of the field-of-view (FOV) without loss of resolution, aiding visualization and interpretation of microscale features across macroscopic areas of tissue.

After an exhaustive study of the state of art, we came to the conclusion that the number of studies applying stitching to HS images in the literature is very limited. Lang *et al.* developed a multichannel mosaicking algorithm which could process square cubes up to 10 channels and 94% overlap between them. It was hypothesized that input parameter could be optimized and still obtain accurate results (e.g. overlap between frames or number of channels per frame).

Finally, the algorithm of Lang *et al.* was proven to produce accurate stitching results for brain histology images when introducing 3 frames at 67% overlap (SSIM of 0.78 for RGB images). This meaning, that to be able to obtain good results, 3 by 3 (9) frames have to be introduced in the algorithm to be stitched, and moreover, each frame has to be 67% overlapping with its predecessor. At the same time, single band stitching was performed. It was proved that the wavelengths giving the most accurate overlaps were in the range of 650-750 nm (SSIM of 0.93 as maximum value). Finally, cubes of 10 and 3 bands were made, with SSIM values higher than 0.75 and wavelengths between 650 and 750 nm. The mosaics resulting from these cubes gave SSIM values between 0.88 and 0.94. All the tests performed were repeated on breast histology images to prove their repeatability.

Key Words

Hyperspectral Image (HSI), whole slide image (WSI) and stitching (mosaicking).

Resumen

Hoy en día, el estudio de *slides* de histología se considera un paso clave para el diagnóstico clínico del cáncer, y la tendencia es digitalizar *slides* de histología para su posterior análisis. Los histopatólogos se dedican a examinar visualmente las regularidades de las formas de las células y la distribución de los tejidos, para luego decidir si las regiones de los tejidos son cancerosas y en tal caso, determinan el nivel de malignidad. Sin embargo, la interpretación de estas imágenes es a menudo subjetiva debido a limitaciones en la visión humana para distinguir diferencias sutiles de color.

La tecnología espectral mejora el rendimiento de la cámara en color al expandir el número de canales más allá de la paleta RGB (Red-Green-Blue). La gran cantidad de información (espacial y espectral), proporcionada por una imagen hiperespectral de una escena, se puede analizar para detectar, identificar o discriminar objetos y patrones, así como la composición química del material presente en la escena. Sin embargo, la información espacial proporcionada por una imagen hiperespectral o multiespectral suele ser menor en comparación con una RGB. Hacer un mosaico (*stitching*) de pequeñas imágenes, permite la expansión del campo de visión (FOV) sin pérdida de resolución. Esto ayuda a la visualización de características a escala microscópica de áreas macroscópicas de tejido.

Después de un estudio exhaustivo del estado del arte, llegamos a la conclusión de que el número de estudios que aplican *stitching* a imágenes hiperespectrales en la literatura es muy limitado. Lang *et al.* desarrollaron un algoritmo de *multichannel stitching* que puede procesar cubos hiperespectrales cuadrados de hasta 10 canales y con una superposición entre ellos del 94% entre ellos (es decir, dos cubos contiguos contienen el 94% de la misma información). En este trabajo fin de máter se planteó la hipótesis de que los parámetros de entrada podrían optimizarse y aun así obtener resultados precisos (por ejemplo, la superposición entre cubos o el número de canales por cubo).

Finalmente, el algoritmo de Lang *et al.* demostró que produce resultados de *stitching* precisos para imágenes de histología cerebral cuando se introducen 3 cubos con una superposición del 67% (SSIM de 0,78 para imágenes RGB). Esto significa que, para poder obtener buenos resultados, se deben introducir 3 por 3 (9) cubos en el algoritmo, y, además, cada cubo debe tener una superposición del 67% con su predecesor. Además, se realizó un *stitching* de cada banda por separado. En este paso, se demostró que las longitudes de onda que daban los mosaicos más precisos estaban en el rango de 650-750 nm (SSIM de 0.93 como valor máximo). Finalmente, se hicieron cubos de 10 y 3 bandas, obteniendo valores SSIM superiores a 0,75 con longitudes de onda entre 650 y 750 nm. Los mosaicos resultantes de estos cubos dieron valores SSIM entre 0,88 y 0,94. Todas las pruebas realizadas se repitieron en imágenes de histología de mama para demostrar su repetitividad.

Acknowledgments

In the following lines I would like to thanks all those people who have guided and supported me throughout this remarkable year.

To my supervisors, Gustavo, Samuel and Himar for trusting me for this project and guiding me all time.

To my parents and siblings, for the constant unconditional support they have given me throughout this year.

To my friends and colleagues who have helped me through this Master Degree and have made it a unique experience.

Content Index

Figures Index

Tables Index

Chapter 1: Introduction

In this introductory chapter of this Master Thesis, the motivation that led us to develop this project is going to be described, as well as the impact that would have on our society and the objectives that are going to be achieved.

1.1. Motivation

A tumor is a growth of abnormal cells in a tissue. These can be malign or benign, that is cancerous or non-cancerous, respectively. For the purpose of these Master Thesis, we are going to investigate brain tumors. Brain tumors can be divided into two main types: primary, which starts in the brain, or metastatic tumors, which begins somewhere else in the body and move to the brain [1]. Treatment includes cautious waiting (monitoring without administering any treatment until symptoms occur or change), surgery, radiation, chemotherapy and targeted therapy. Targeted therapy uses medications or other substances to fight specific cancer cells that cause less damage to normal cells. Most people receive a combination of these methods [2].

Before any treatment is made, a diagnostic must be performed. Medical doctors diagnose these tumors through a neurological examination and other kind of tests such as magnetic resonance imaging (MRI), computed tomography (CT) or pathologically analyzed biopsies. Moreover, automatically detection of these tumors can be achieved by using hyperspectral imaging (HSI) of histology slides, instead of biopsy observation under a microscope.

Images can be classified according to the number of bands they contain. While RGB images capture three discrete wavelengths within the visible range of the electromagnetic spectrum, multispectral (MS) images are able to capture information up to dozens of bands, and hyperspectral (HS) images contain more than 100 bands within and beyond the visible range [1]. To obtain a hyperspectral image, the sensors measure the reflected radiance (reflectance) in a large number of wavelengths, thus, creating a high spectral resolution image. The bands captured are grouped to produce a hyperspectral cube, which is a 3D data structure whose dimensions are the combination of the spatial (x, y) and the

spectral (l) information of the scene. Capturing images with high spectral resolution defines the concept of HSI [3].

The main strength of HSI over multispectral imaging is the large number of adjacent spectral bands which are possible to acquire and handle, allowing detection of materials in a scene with higher precision. If the radiation reflected to the sensor is measured at different wavelengths over a region, a spectral signature of such region is obtained. That is, a representation of each image pixel is obtained along the spectrum. This representation creates a unique footprint of the material that allows us to identify such different materials with accurate precision [4]. Thus, this type of images and the type of information they provide have multiple applications in fields such as remote sensing [4], medicine [5] or agriculture [6].

In this project, we will use a hyperspectral camera to obtain images with the help of a microscope with hyperspectral capacity [7]. The problem associated with this type of images is that the different magnifications provide different types of information about the sample. The acquisition of images at high magnifications is necessary to identify the morphological details of cells. These morphological details are of great importance for the final diagnosis of the sample in histological applications. In addition, since the sample size is larger than the area that can be captured in a single image, it is necessary to use algorithms that are capable of unifying them in a larger image, this procedure is known as stitching [8].

One of the challenges of using hyperspectral images for microscopic sample analysis is that several small images of large spatial resolution have to be captured and assembled (stitching) to achieve the complete image from the sample. Stitching is the process by which multiple photographs with overlapping fields of vision are combined to produce a high-resolution image. This process is commonly done through the use of certain software or algorithms to achieve an almost exact overlap between images, producing a uniform result. The union of images has many applications at the moment, as it is in medical images [9], photomosaic [10] and photosatellites [11].

However, this mosaicking of images is not trivial. Algorithms need to be developed to perfectly combine overlapping images, even in the presence of some problems that are commonly encountered when multiple images are going to be assembled. An error in a medical image, such as the movement of the scene or the difference in exposure to light between the images, can lead to an error in the diagnosis, with dramatic consequences [8].

1.2. Context

This Master Thesis was developed within the research line of hyperspectral imaging (HSI) acquisition and processing for medical applications that is currently carried out by the

Division of Integrated Systems (DSI) of the University Institute for Applied Microelectronics (IUMA) of the University of Las Palmas de Gran Canaria (ULPGC), specifically in the field of pathological analysis of brain cancer biopsies.

In addition, IUMA has been involved in projects financed by both public and private entities, in the field of processing HS images in different areas. Among these projects are:

1.2.1. HELICoiD Project (CNET-ICT-618080)

Helicoid was a European collaboration project between four universities (ULPGC, Imperial College of Science, Technology and Medicine of London, Polytechnic University of Madrid, Assosiation pour la Recherche et le Développement des Methodes et Processus Industriels de Paris - Armines), three industrial partners (Medtronic Iberica SA, General Equipment for Medical Imaging S.A., Virtual Angle B.V.) and two hospitals (Canary Foundation for Research and Health, University Hospital of Southampton NHS Foundation Trust), financed by the Executive Research Agency (REA) of the European Union [9].

The purpose of this project was to develop a demonstrator capable of differentiating between healthy and tumor tissue in real time during neurosurgery interventions by means of hyperspectral images, thus enabling real-time resection of tumor tissue to be confirmed in real time, avoiding excessive resection of adjacent healthy tissue and indeterminations due to displacement of brain mass. This project ended in December 2016.

1.2.2. ITHaCA Project (ProID2017010164)

After HELICoiD project finished, the ITHaCA project was created to continue with the investigation of intraoperative brain cancer diagnosis. This Master Thesis is framed within the ITHaCA project (IndenTificación Hiperespectral de tumores CerebrAles), funded by the Canarian Agency for Research, Innovation and the Information Society of the Canary Islands Government [7]. This is a multidisciplinary project that integrates engineers, neurosurgeons and pathologists. Its main objective is to perform a real-time accurate differentiation and classification by using hyperspectral images of different types of brain tumors. This fundamental research project is promoted by the IUMA (University Institute of Applied Microelectronics) of the University of Las Palmas de Gran Canaria and FUNCANIS (Canarian Foundation for Health Research), the research management foundation of the University Hospital of Gran Canaria Doctor Negrín (HUGCDN).

For the purpose of this Master Thesis project, it is proposed to perform the stitching of several images taken with the hyperspectral microscope acquired by the University Institute for Applied Microelectronics (IUMA). This is, until the moment, the only known microscope with hyperspectral capacity in the range of 400 to 1700 nm that it is used for pathology images in Spain. Due to the different magnification factors existing, it is proposed as principal task the stitching of these hyperspectral images for its future processing. This task will involve solving complex problems associated with the registering of images, the

maintenance of brightness levels and the spatial consistency among images (seamless). The resulting image must conserve the original characteristics as if we had taken just one complete image. This way, we assure that the posterior automatic detection of brain tumors will come up with a coherent diagnostic for pathologists.

1.3. Objectives

The main objective of this Master Thesis is to adapt a stitching algorithms of large spatial resolution images for automatic assembly of hyperspectral histological images captured with the pathological microscope available in the research group infrastructure. This main objective can be broken down into several specific objectives that must be performed along this project.

- **O1.** To study the actual state-of-art algorithms currently used in the literature for image stitching.
- **O2.** To study the HSI technology, its application in the medical field, and the use of the hyperspectral microscope instrumentation available in the laboratory.
- **O3.** According to the information collected from the stitching algorithms and the performance of hyperspectral images, the optimal conditions used to capture the microscopic hyperspectral images will be proposed, in order to perform an efficient stitching.
- **O4.** To develop image stitching algorithms through the high-level language MATLAB®.
- **O5.** To apply the developed algorithms to the stitching of hyperspectral microscope images of histological samples for the future use of this images in the detection of tumors at different magnifications.
- **O6.** To validate the results obtained using appropriate quantitative and qualitative metrics and compare the results of the HSI stitching versus the stitching of conventional digital pathology images.
- **O7.** Estimation of the computational cost of the algorithms developed for future hardware implementation.

Conclusions

In this section, it has been explained the motivation that drove us to carry out this project at the same time as the impact that the results would have in our society and the objective we wanted to fulfill.

Chapter 2: Background

In this second chapter of the Master thesis, it is going to be described in first place what is pathology and histology and the important role they play when dealing with brain tumors. Furthermore, spectral technology is also going to help in the diagnosis of these kind of cancer by using whole slide imaging. However, resolution problems arise when digitalizing histology slides and thus, stitching have to be applied.

2.1. Pathology

Pathology is defined as the study of diseases and it brings together science and medicine to improve patients care. Pathology doctors and scientists are experts in illness and disease and their work encompass from diagnostic testing and treatment advice to cutting-edge genetic technologies and preventing diseases. Pathologists have played a critical role in research, advancing medicine and devising new treatment to fight viruses like blood transfusion, vaccination and treatment of inherited conditions, among others. Thank to this discipline, illnesses have been significantly reduced during the last 100 years [12].

As previously said, the main goal of this science is to determine the causes and effects of the different diseases and to achieve that samples of body tissue have to be examined. Commonly, hospitals have their own teams of scientists who study different samples of patient's bodies to try to understand what is causing their disease. These teams are made up of pathologists as well as biomedical scientists and support staff. Doctors, nurses, surgeons, and other medical staff look to pathologists and consultant clinical scientists for advice on the nature and seriousness of a patient's illness, making sure they get the most appropriate treatment.

2.1.1. Histopathology

Histology studies microscopic structures of biological material and the ways in which individual components are structurally and functionally related. It is a key discipline for

biological and medical science because it brings together different health branches such as biochemistry, molecular biology and physiology [13].

Histopathology has roots in both clinical medicine and in basic science. Its main purpose is to study the diseases by examining the tissues or cells under the microscope. Histopathologists work closely to other clinician's specialties being their task to make the diagnosis of tissues and helping clinicians managing patients' care. They can reach a diagnosis by examining a biopsy which is a small piece of tissue, for example from the skin, liver, kidney or other organ. Their job is to carefully examine the tissue under a microscope, looking for changes in cells that might explain what is causing a patient's illness [14].

As we can see in Figure 1, biopsy samples can be acquired from many areas of the body by using safe instruments such as:

- Scalpels for directly accessible tissues such as the skin, mouth, nose, etc.;
- Needles into solid organs;
- Endoscopic tubes into the alimentary tract or body cavities;
- Special flexible cannula inside blood vessels.

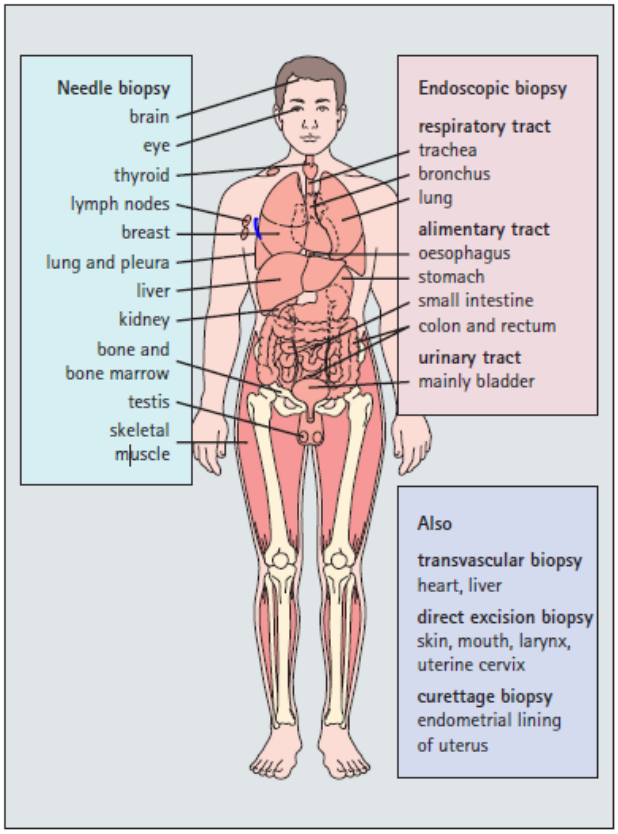

Figure 1. Different techniques to obtain small samples of many areas of the body [13]**.**

Furthermore, it has to been taken into account that knowledge of normal histological appearances is essential if abnormal diseased structures are to be recognized, and to comprehend how abnormal biochemical and physiological processes result in disease.

2.1.2. The Advance of Histology

Histology was first studied using a simple light microscope and elemental techniques for preparing thin slices of biological material to be able to examine them. Despite the simplicity of the method employed, early histologists acquired a huge amount of information related to the structure of the biological materials under study. These first studies led Rudolf Virchow to enunciate his cellular theory of the structure of living organisms that established the cell as the basic building block of most biological material [15].

In those early years, a vocabulary of histology was developed, build on light microscopic analysis of cells and limited understanding of cell physiology. Assembly of cells having analogous morphological characteristics were described as forming tissues. These were first divided just into four types: epithelial, muscular, nervous and connective tissues [13].

Modern investigations have revolutionized our understanding of cells, and thus the science of histopathology. Modern techniques include electron microscopy, cloning of cells in culture, protein sequencing and molecular genetics, among others. However, and despite the rapid emergence of the science, terms and classifications were not changed much since original histological studies were performed. A rigid classification of cells and tissues was maintained during years.

Fortunately, this rigid histological system is now giving way to a more exciting and functional approaches, using all the information available of cell biology [13]. We are living an exciting period in histology, where we are able to explore the physiological and molecular basis of biological structures through the development of techniques that allow us to examine the chemical make-up of living tissues under the microscope. It is now becoming clear why various biological structures are shaped and arranged as they are.

Nowadays, the study of histology slides is regarded as the gold standard for the clinical diagnosis of cancer, and the trend is to digitalize histology slides for further histology image analysis [16]. In histology image analysis for cancer diagnosis, histopathologists visually examine the regularities of cell shapes and tissue distributions, decide whether tissue regions are cancerous, and determine the malignancy level. Such histopathological study has been extensively employed for cancer detection and grading applications, including prostate [17], breast [18], cervix [19], and lung [20] cancer grading, neuroblastoma categorization [21], and follicular lymphoma grading [21]. For the purpose of this thesis, we are going to use histopathologic samples of brain tumors.

2.2. Brain Tumors

World Health Organization (WHO) defines cancer as "a large group of diseases that can start in almost any organ or tissue of the body when abnormal cells grow uncontrollably, go beyond their usual boundaries to invade adjoining parts of the body and/or spread to other organs" [22].

Tumors of central nervous system (CNS) include the tumors of the brain and spinal cord, as well as their covers. Those tumors are uncommon tumors, accounting for approximately 1% of all human body tumors [23]. Brain tumors are assigned into four grades, from Grade I very benign tumor to Grade IV highly malignant tumors. Diagnosis of brain tumors is primarily based on the WHO Classification of Tumors of CNS [2]. This expert consensus scheme was first completed in 1979 and then revised in 1993, 2000, and 2016. This scheme is currently the most widely utilized by neuropathologists worldwide for typing and grading the CNS tumors.

In Figure 2, it is depicted a basic classification of brain tumors based on the one previously mentioned. They can be divided into two main types: primary which starts in the brain, or metastatic which begins somewhere else in the body and it moves to the brain.

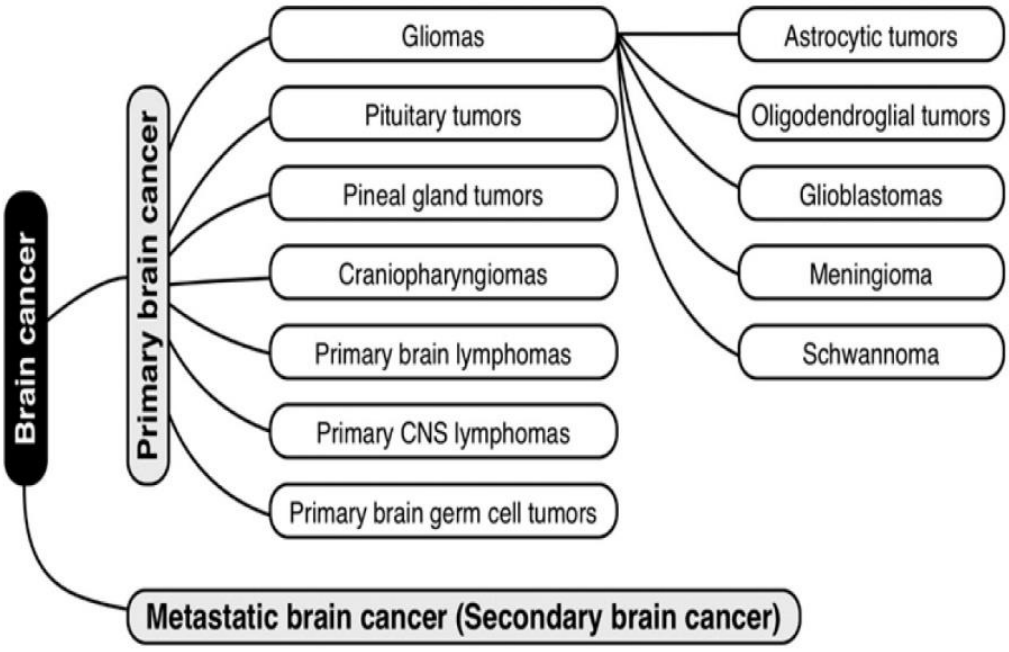

Figure 2. Basic classification of Brain Tumors [24].

The most common primary brain tumors are gliomas, pituitary adenomas, and vestibular and primitive neuroectodermal tumors. Gliomas are tumors that begin in the glial tissue and they include glioblastomas, astrocytomas, schwannomas, oligodendrogliomas, and others. The most common malignant brain tumor is glioblastoma (GB, 81% of malignant

CNS tumors), which is usually associated with poor prognosis. GM is classified as a subtype of astrocytoma. GM is classified as grade IV according to the WHO. With regard to treatment, GM and grade III brain tumors are managed similarly.

Any intracranial tumor, regardless of the degree of malignancy, can potentially invade or displace critical brain areas, resulting in neurologic compromises. The most common complications are seizures, peritumoral edema, venous thromboembolism, fatigue, and cognitive dysfunction [24].

2.2.1. Molecular Diagnosis of Adult Gliomas

Glial tumors comprise approximately 25–30% of primary CNS tumors and represent a spectrum ranging from low-grade, benign to the highly aggressive, malignant tumors. They are broadly classified by glial cell type of origin and determined by histology with or without the use of immunohistochemistry (IHC), which is then used to provide a WHO grade [2].

However, histology has not been able to accurately predict response to treatment or clinical outcomes, and it is not uncommon for many of these tumors with nearly identical histologic features to have very different outcomes [23]. As a result, there is a need of obtaining better histology images, with more information, to improve their further analysis.

2.3. Spectral Technology Applied to Tumor Detection

Conventional histopathology relies on stained tissue cell specimens viewed by an optical microscope with transmission illumination. The introduction of fluorescence microscopy techniques has added the ability to examine cell condition and function in addition to structure in research and clinical diagnosis methods, such as immunochemistry. However, interpretation of these images is often subjective due to limitations in human vision to distinguish subtle color differences particularly because of spatially overlapping emissions. Spectral technology improves on color camera performance by expanding the number of channels beyond the RGB palette [25].

2.3.1. Basics of Spectral Imaging

First of all, two basics concepts can be differentiated when working with light. In one hand, *Irradiance* refers to the energy of light per unit time incident on a surface, normalized by the surface area (W/m^2). On the other hand, *Reflectance* (light reflected) is a dimensionless number between 0 and 1 that characterizes the incident fraction of light reflected by a surface [3].

The characteristics of sunlight reflection from a material contribute to the own material's detection and classification within of a scene. When a material is irradiated, it absorbs

$L_\alpha(\lambda)$, transmits $L_\tau(\lambda)$ and reflects $L_r(\lambda)$, light in a particular way. All the components are based on wavelengths (1).

$$L_i(\lambda) = L_\alpha(\lambda) + L_\tau(\lambda) + L_r(\lambda) \quad (1)$$

The proportions of $L_\alpha(\lambda), L_\tau(\lambda)$ and $L_r(\lambda)$ in (1) vary according to spectral behavior of the different materials found within the surface of the Earth. Spectral variations captured by the sensor allows us to detect or classify an object in an image. (2) allows us to quantify the reflectance ρ_i, measuring the amount of incident irradiance $L_i(\lambda)$ which is reflected, $L_r(\lambda)$.

$$\rho_i = \frac{L_\tau(\lambda)}{L_i(\lambda)} \quad (2)$$

The variation of the reflectance ρ_i as a function of the wavelength is called the spectral signature, which is the quantitative measurement of spectral properties of an object in the range of the electromagnetic spectrum collected by a sensor (Figure 3). Thus, spectral sensors detect reflected solar energy by the different materials and measure the intensity of the energy reflected in different wavelengths of electromagnetic spectrum creating the spectral images. These images contain spatial (x, y) and spectral (λ) information, forming 3D hyperspectral cubes. As we can see in Figure 3, each pixel (x, y) contains a spectrum with high spectral resolution called spectral signature.

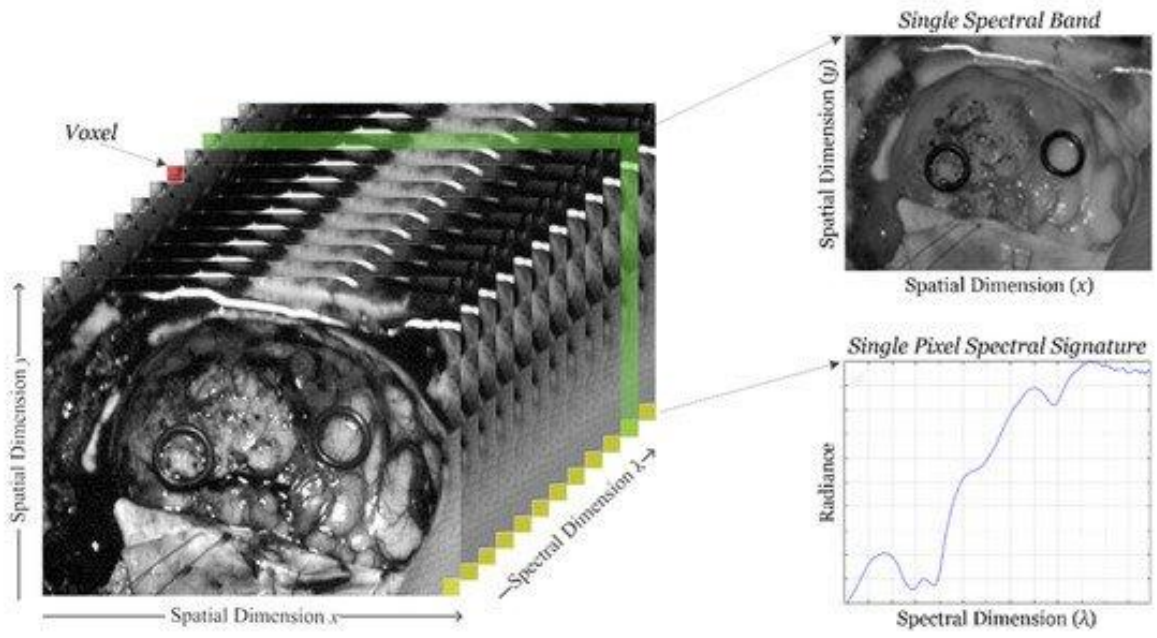

Figure 3. Hyperspectral cube concept and spectral signature of a specific pixel [5].

2.3.2. Multispectral and Hyperspectral Imaging

Spectral resolution is determined by the number of spectral bands and the width of them, used to measure reflection at different wavelengths. Figure 4 shows that spectral images can be classified according to the number of bands they contain: red-green-blue (RGB) or visible (VIS), which belong to the visible range of the spectrum; multispectral, which capture information in only dozens of bands, and hyperspectral, which contain more than 100 bands [25].

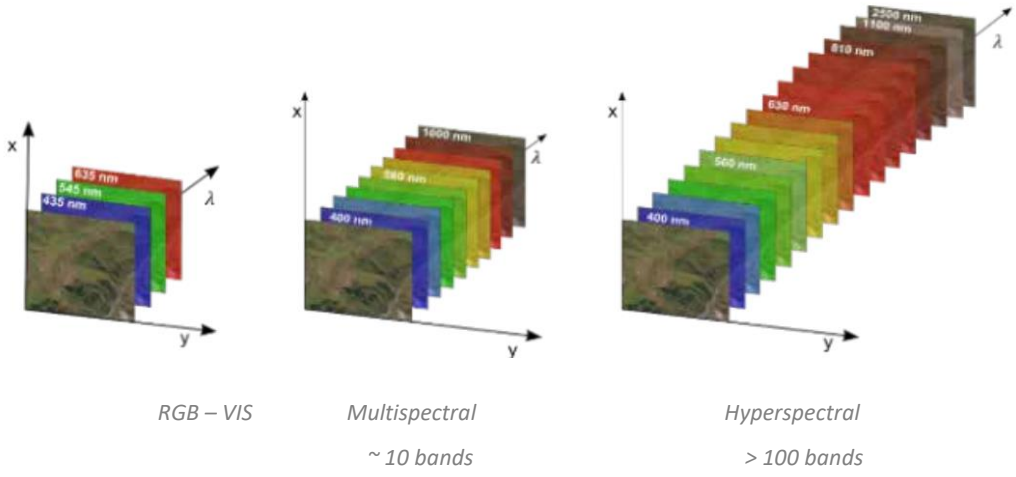

Figure 4. Classification of the spectral images. These are differentiated by the number of bands and the width of these [11]**.**

HSI main strength over Multispectral Imaging is the large amount of contiguous spectral bands possible to acquire and handle, allowing a precisely detection of materials in a scene. Figure 5 illustrates the superiority in spatial and spectral resolution of HSI over MSI, producing an image with more information.

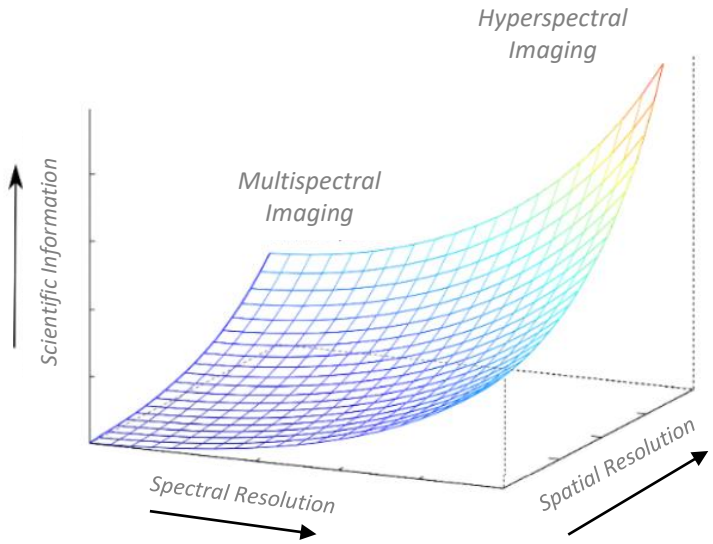

Figure 5. Graphical differentiation between MS and HS images. For the aim of the comparison, it is taken into account the spectral and spatial resolutions as well as the data content of each type [3]**.**

The greatest content of information of HSI based on spectral resolution improves and expands its use and exploitation. It allows the development of target detection algorithms based on the spectral signature of the target to be detected (e.g. tumor tissue) [26].

2.3.3. HSI/MSI Applications for Histopathological Sample Analysis

HSI is an emerging technology in the biomedical field. In the recent years, many researchers have explored this technology as a diagnostic aid tool for different applications. Compared to other existing technologies for assessing the diagnosis, one of the strengths offered by HSI is being completely non-invasive [27]. In medical applications, this technology has been employed in a wide range of fields, including blood vessel visualization enhancement [28], intestinal ischemia identification [29], measuring the oximetry of the retina [30], estimating of the cholesterol levels [31] or cancer detection [32], among others.

Regarding studies for clinical diagnosis of histological samples, the number of studies using hyperspectral data in the literature is limited. Ortega *et all.* [33] performed a systematic review, based on the use of both HSI and MSI for pathological diagnosis, digital staining and other applications. According to the different fields within medical diagnosis, they analyzed a total of 84 research articles in the field of hematology, breast, central nervous system, gastrointestinal, genitourinary, head and neck, and skin. Some examples these investigations are the identification of acute lymphoblastic leukemia [34], blood cell analysis [35] or mitotic cell detection and segmentation [36].

Furthermore, we can see the workflow of a specific study carried out by Ortega *et all.* [27] who studied the detection of brain tumor in pathological slides by using HSI. In their research work, HS images from pathological slides belonging to human brain tissue suffering high-grade gliomas were analyzed. The main goal of their study was to analyze if it is possible to discriminate between normal and tumor tissue in pathological slides by processing only their spectral information.

In Figure 6, the processing framework of this study is explained. First, raw images were acquired by using a HS sensor. Then a multiple steps pre-processing chain was applied to the data. And at the end, three different classifiers were employed to automatically distinguish between tumor and normal tissue, using as features only the spectral information.

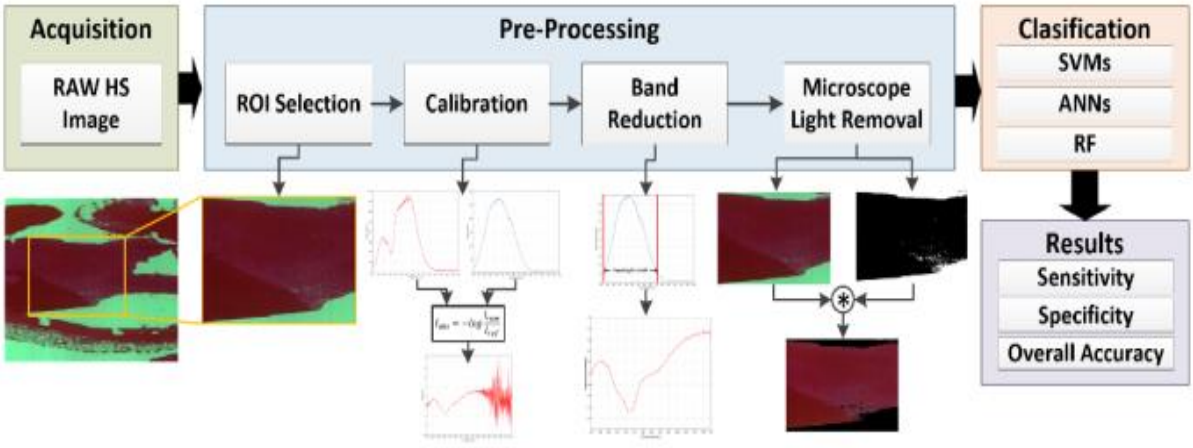

Figure 6. Processing framework block diagram [27]**.**

The results obtained showed competitive results in the discrimination between normal and tumor tissue, regardless of the classifier employed. Thus, HSI proved to be a suitable technique to develop a future automatic diagnostic tool for pathological slides [27].

At the end, according to the results depicted in the aforementioned investigation and the other 83 analyzed research articles, *Ortega et all.* [33] concluded that there are still many challenges that have to be addressed for the final adoption of HSI/MSI for digital pathology in a clinical setting. Firstly, the spectral acquisition equipment is unstandardized, complex, research-grade, and expensive. Additionally, the analysis algorithms are often different. Thus, the experimental results reported in the literature are difficult to compare. Moreover, it is extremely difficult to extrapolate the results obtained in one particular diagnostic application in one specific organ system to another application/organ, mainly due to the heterogeneity of the spectral properties of the different tissues. The use of HSI/MSI for digital and computational pathology is promising and is still in its infancy, requiring more investigation and creative solutions to the problems for its clinical translation [33].

However, overall, HSI/MSI technologies are able to succeed in histological disease detection. Diagnostically important spectral features can be subtle and not easily assessed by the naked eye, but HS sensors capture such features from the image scene for a deeper understanding and analysis [33]. Finally, HSI technology coupled with microscopy is now finding a broad set of application areas including disease diagnostics by digitization of histology slides and its storage in digital form [26]. Consequently, digitized tissue histopathology has now become amenable to the application of computerized image analysis and further machine learning techniques.

2.4. Whole Slide Imaging (WSI)

Whole slide imaging (WSI) refers to the digitization of entire histology slides or specific areas. WSI has revolutionized the pathology field, making it a necessary first step for a wide array of digital tools to enter the field. As just explained its basic function is to digitize glass slides, but its impact is much higher. It is an improvement for pathology workflows, reproducibility, dissemination of educational material, expansion of service to underprivileged areas, etc. Another application that has also taken advantage of this technology is the intra-institutional and inter-institutional collaboration being a significant innovative movement with far-reaching effects [37].

As explained in section 2.1, pathology relies on the accurate examination of microscopic images in order to precisely diagnose patients and manage therapeutic decisions. With the appearance of whole slide imaging, pathologists have begun to carry out the act of histology slides examination in the computer screen instead of direct observation in the microscope, as they used to. This technology allows them to navigate a virtual slide, giving on to a number of new opportunities not feasible using conventional microscope such as digital collaboration, integration with electronic workflows and health records, and diagnostic support based on computational tools like artificial intelligence [37].

Although WSI benefits are countless, the adoption of this new technology is not always easy. It remains a difficult step to overpass for many academic centers or research institutions which may do not have an easy access to funds and new material for their laboratories or are unfamiliar with the new technologies and the opportunities they may offer. To apply WSI technologies it is needed a whole slide scanner which basically is a microscope under robotic and computer control. This is attached to a highly specialized camera(s) containing advanced optical sensors. Thus, as we can see in Figure 7, WSI scanners consist of 6 main components: a microscope with lens objectives, a light source, robotics to move glass slides, a digital camera for image capture, a computer and a virtual microscopy viewer (VMV) to see and interact with the images [38].

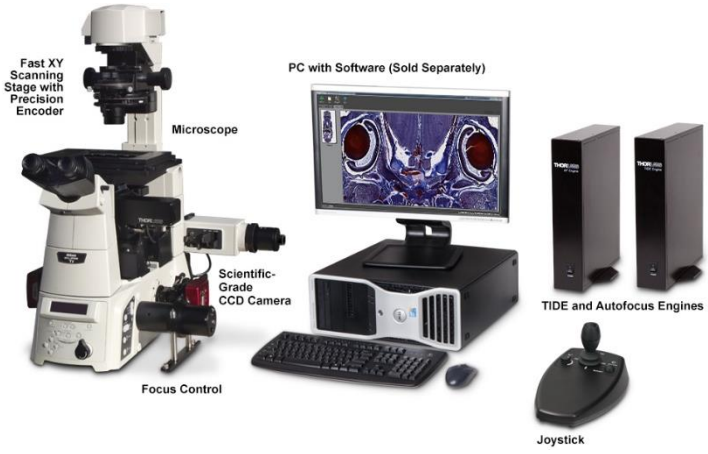

Figure 7. Example of Whole Slide Image setup [39]**.**

The process of slide digitization is shown in Figure 8. It starts with the image acquisition or scanning by the camera sensor followed by its assembly to generate a digital image of the whole slide. Then, the multiple images obtained are stored on the computer. And finally, the WSIs are displayed on a virtual microscopy viewer [39]. However, construction of such a VMV implies to solve different kind of problems, whose nature depends on the different involved steps: assembling the high-resolution image, efficient storage and rapid information availability for navigation. These three general requirements define three complementary processes [40].

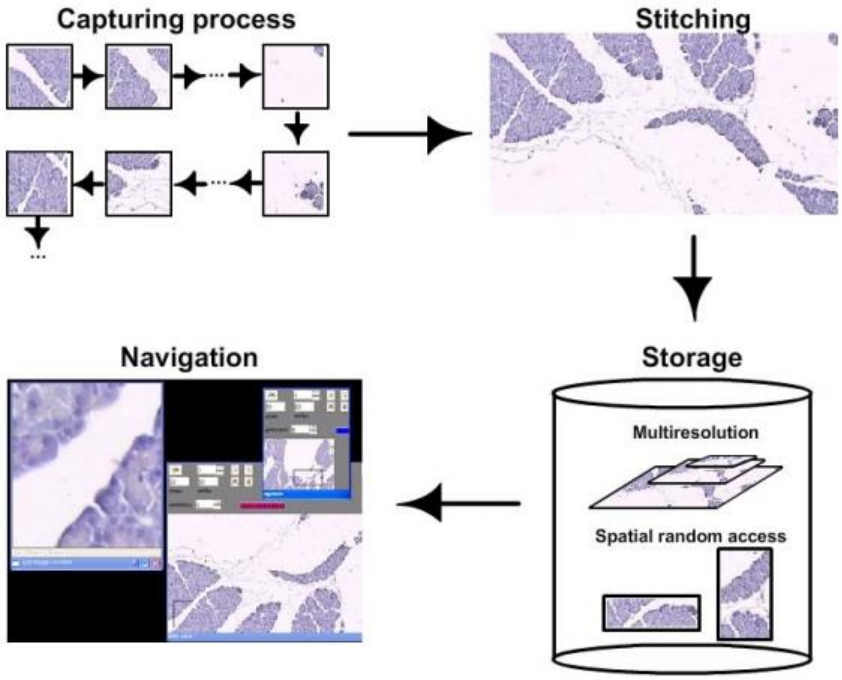

Figure 8. The whole scheme illustrates the Virtual Microscopy process [40]**.**

Stitching is a fundamental step in the process since acquiring the area of the whole slide in just one image usually does not provide much spatial resolution. Spatial resolution is defined as the minimum distance at which two distinct objects can be identified as separate events [37]. For example, in Figure 9 we can see that in the second image (5 m resolution) changes are distinguished every 5 meters but, in a 30 m resolution image changes are less detected, making a lower resolution image of the same area

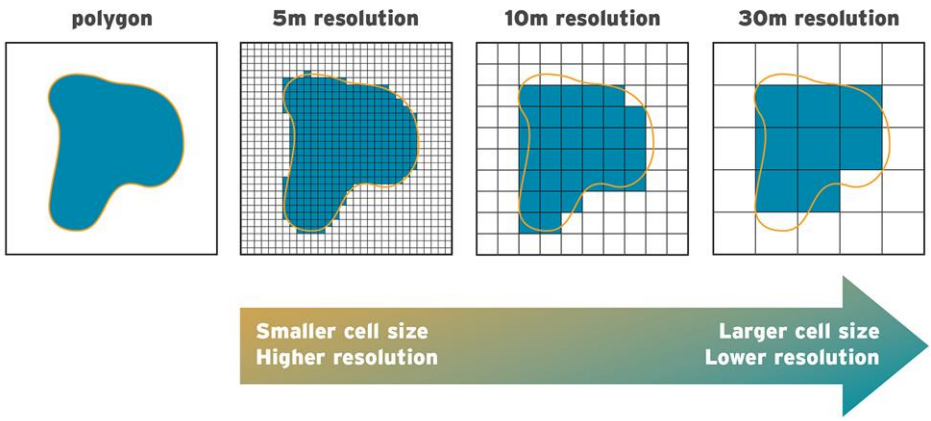

Figure 9. Example of different spatial resolution representing the same polygon [41].

The resolution problem can be achieved by scanning different higher magnification FOV which will be later assembled into a single high-resolution image.

Furthermore, clever storage strategies are needed since the virtual slide demands a huge amount of memory space. For this reason, it is required an intensive use of image compression methods but subjected to the restriction that such methods must also allow an efficient access to information when required. Additionally, compression in medical images must be lossless since minimal distortions may lead to a false diagnosis [42].

Finally, navigation is the process which permits a user to carry out a microscopic examination of a particular sample as it would be possible using a conventional microscope. This virtual microscope must allow sequential and random translational movements at any of the XY-axes or zooms when moving along the Z-axis [43].

In conclusion, mega-images, understood as whole-slide-images, are constructed by a sequential capturing process. They shall be in the very near future a useful tool in most routine microscopical applications. They allow a unique image storage, called virtual slide which makes possible a so far unknown information availability for image retrieval in case of latter studies, medical training, distribution by electronic media, image exchange between pathologists, annotation capabilities and morphometrical measurements [40].

2.5. Image Stitching

In biomedical and clinical studies, it is often highly desirable to observe images of whole tissue sections with high resolution. However, it is usually difficult to get a single image with high resolution to view a whole sample. A common solution to this problem is to stitch several images with FOV, which will have higher spatial resolution, to form a composite one. As we can see in Figure 10, image stitching is highly desirable to acquire a high FOV image which represents macroscopic areas of certain structures or whole sections, while retaining microscopic resolution [44].

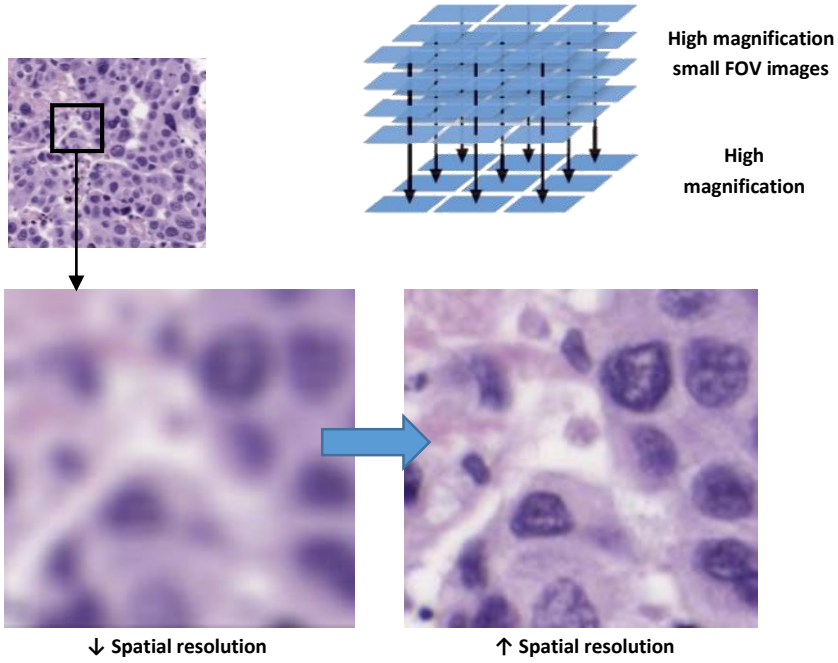

Figure 10. Example of increasing the resolution of an image thanks to the use of the stitching technique.

This process is commonly performed through the use of certain software to achieve almost exact overlaps between the images, producing a uniform result [45]. The way in which most microscope digital cameras, which have stitching capacity, work is the following:

1. While focusing on the sample with the camera turned on, the software is opened.
2. The image stitching feature captures multiple images while the mechanical stage is slowly moved in both the X and the Y axis to cover the field of view desired.
3. The software works in the background to stitch this larger image together.

However, creating a large mosaic is challenging because the stitching algorithm consume a lot of computational resources, needed for assembling the resulting mosaic. In addition, algorithms working on the software need to be developed to seamlessly combine overlay images, even in the presence of problems. Some commonly problems encountered when assembling multiple images are: parallax, that is, the displacement in the apparent position of an object; lens distortion deflecting light rays; the movement of the scene; and the difference in light exposure between the images [45].

Anyway, since quantitative pathologic examination of cells and tissues can provide important diagnostic and prognostic information, accuracy is necessary on the macroscopic image and thus, precise stitching methods are required [46].

2.5.1. Stitching of HS/MS Images

The spatial and spectral information provided by a HS image of a scene can be analyzed to detect, identify, or discriminate objects and patterns as well as the chemical composition of the material present at the scene [9]. However, spatial information provided by one

HSI/MSI frame is usually lower compared to traditional RGB frame. Microimage stitching (mosaicking) offers an approach for expansion of the FOV without loss of resolution, aiding visualization and interpretation of microscale features across macroscopic areas of tissue. In Figure 11 it is shown how stitching improves the spatial range for both, HS and RGB, images at the same time that allows HS/MS images to have more spectral information [47].

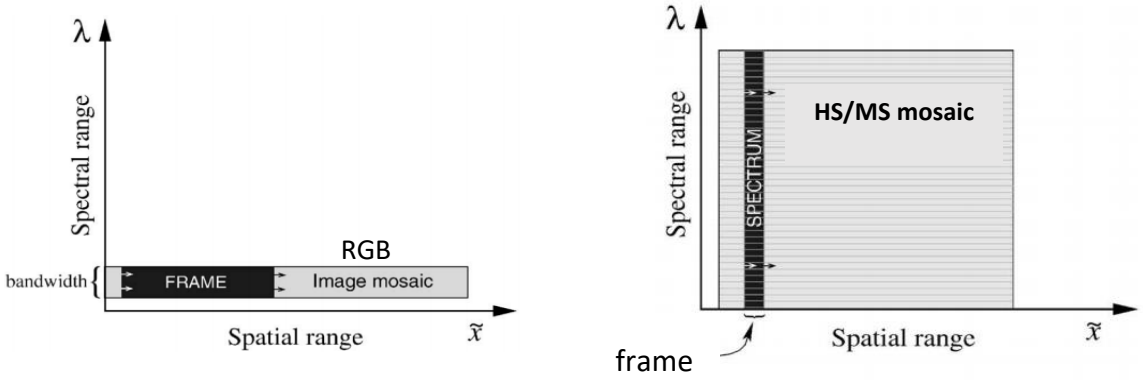

Figure 11. Stitching of a RGB image (left) vs HS/MS image (right). Mosaicking HS/MS data allows for high spectral and spatial range images.

In conclusion, mosaicking can be used for enhancement of the FOV of HS/MS images [48]. This way it is possible to increase the amount of information acquired via HSI and, therefore, to increase the possibility of data analysis. However, the biggest challenge in this process is the mapping of the images of the individual spectral channels to each other (co-registration). Therefore, an investigation should focus on the procedure of data acquisition, correction and registration.

Conclusions

In this section, the main motivation for the study of histological slides has been described, which is considered as the gold standard for the clinical diagnosis of cancer. Specifically, we have focused on brain tumors and its better detection by using HS images. Furthermore, it is possible to couple this HS technology with a microscopy, allowing histology digitalization for further data analysis. However, HS spatial resolution is usually low compared to RGB imagery. We propose to stitch high-magnification, high-resolution HS frames, generating a large FOV HS mosaic. This way we will increase the information available and the possibility of further histology image analysis and cancer detection.

Chapter 3: State of Art

In this chapter the latest image stitching methods used for digitalizing microscope slides is introduced. The advantages and weaknesses of these algorithms are going to be described. Finally, we will hypothesize a potential solution.

3.1. Current Situation

Optical biopsy of disease is becoming a key element for basic biology research. However, cellular resolution generally comes with the trade-off of a microscopic FOV, as clinicians may need to survey large (macroscopic) areas. Consequently, achieving both microscopic resolution and macroscopic FOV optical imaging remains a central challenge in the field.

Microimage mosaicking offers an approach for expansion of the field-of-view without loss of resolution, aiding visualization and interpretation of microscale features across macroscopic areas of tissue. Mosaicking is an image analysis technique in which sequential frames from a sequence of images are examined for common spatial features and then stitched together by overlapping the images' shared regions pairwise.

Adequate microscopic virtual reconstruction of a desired part of a biological sample is achieved using image registration and stitching. In the virtual microscopy context, registration is the process of finding the amount of overlay between two neighbor frames by maximizing a particular similarity measure between them. Two kinds of similarity measures have been used in virtual microscopy systems [40]:

- Area based methods. These measures are based on the similarity of intensities between the two neighbor FOV, using their intersected regions. They are based on low-level image intrinsic properties and therefore they are very sensible to the type of noise.
    - Sum of squared differences. Thévenaz *et al*. have used the sum of squared differences as similarity measure in a virtual microscopy system [49]. This measure has shown to be appropriate in many applications since it is simple and optimal under controlled conditions i.e. when differences between

images are exclusively caused by Gaussian noise [50]. However, inter-image intensity variations are mostly linear in histological applications and constitute the major source of noise [51], together with the unavoidable biological variability and the technical difficulties of any histological procedure.

  - Correlation. In routine microscopy, illumination settings are controlled in such a way that most changes regarding intensities between neighboring FOV can be modelled as linear [52]. Therefore, similarity measures based on correlation such as the normalized cross correlation or phase correlation [53], result more robust and become also more general. They are remarkably less sensible to noise than simple measures at the level of pixel differences such as the sum of squared differences and they are also robust to image displacement or rotations produced by microscope stage instabilities.

- Feature based methods. These approaches are based on the detection of salient features in the image intersection which can be used in a general manner.
  - Corners. Sun *et al.* [54] have proposed a method which finds a set of corners in the overlapping region of each FOV, based on the Harris corner detector method [55], which is followed by a match of the corresponding features. In this case the similarity measure is the Euclidean distance between the corresponding features. Although the method is rapid, this is not general or robust since there is not any guarantee for the corners to exist in every microscopical image.

Summarizing, the registration algorithm determines the best translational offset between two consecutive image frames. In the application we are targeting, virtual microscopy pathology slide mosaicking, illumination settings are usually controlled, and the dominant component of motion is translational, being any non-translational motion small in comparison. That is the reason we chose to implement a correlation area based method previously employed by Bedard *et al.* [56]. Their algorithm, based on the Guizar-Sicairos *et al.* [57], performs an optimized cross correlation using discrete Fourier transforms (DFTs). The cross correlation of two images $f(x, y)$ and $g(x, y)$ is given by (3).

$$r_{fg}(x_i, y_i) = \sum_{u,v} F(u, v)G^*(u, v)exp\left[i2\pi\left(\frac{ux_i}{M} + \frac{vx_i}{N}\right)\right] \quad (3)$$

where N and M are the image dimensions, uppercase letters represent the DFT, and * denotes complex conjugation. The approach to finding the cross-correlation peak is as follows: 1) compute the product $F(u, v)G^*(u, v)$; 2) take the inverse Fast Fourier Transform (FFT) to obtain the cross correlation; and 3) locate its peak [57]. Error of registration fit is given by the normalized root-mean-square error (NRMSE).

After a similarity measure between frames has been selected, the registering phase consists in finding the optimal transformation function which maximizes that similarity between neighboring FOVs. Notice that a large image must be generated by registering hundred or thousand FOV, whereby optimal registration schemes are required (Figure 12). Romo *et al.* [58] decided to implement an strategy following a serpentine pattern as it simulates the microscope's movement while scanning a microscopy slide. Rankov *et al.* [59] proposed to start at the center of the digitalization framework and to follow a spiral-like pattern, under the hypothesis that the image at the center contains the higher information. Appleton *et al.* [51] aligned simultaneous rows of FOV, while images associated to each row are firstly stitched into one single image using an efficient dynamic programming algorithm for solving the optimization problem.

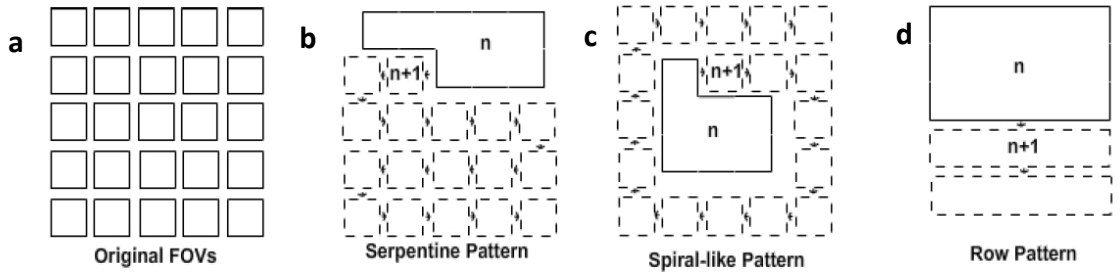

Figure 12. a) Sequence of microscopical FOVs that will be stitched. b), c) and d) Different stitching schemes [40]**.**

In the algorithm we plan to carry out [57], registered high resolution frames are first inserted into a large zero-value image called a canvas. The first frame in a video sequence is copied to the center of the canvas, as in Figure 12.c, and so it follows a spiral-like pattern. Subsequent frames are inserted into the canvas at an offset determined by the registration algorithm. For our application it is important to preserve size and separation of features such as nuclei, so we typically use the dead leaves approach [60], which simply replaces overlapping regions with the new frame. Although individual frame boundaries can become apparent when using the dead leaves approach, spatial features within the image keep their size [56]. Registration errors can occur for several reasons, as when there is little spatial information (such as in uniform grayscale images) or when there is loose debris.

Additionally, the development of hyperspectral and multispectral systems for biomedical applications provides motivation for adapting mosaicking algorithms to process a number of simultaneous spectral channels. The advent of multidimensional imaging techniques provides novel information about frame-to-frame motion that single-mode techniques are not equipped to analyze. Thus, existing mosaicking algorithms should be adapted to leverage spatial and spectral data and enable these techniques to image micro- and macroscopic environments with greater fidelity than their single-channel predecessors.

Lang *et al.* [61] presented a first step in the development of multichannel mosaicking algorithms. They employed a method to characterize the noise tolerance and computational efficiency of stitching algorithms to enable quantification of mosaicking

performance of multichannel images relative to single-channel analogues. When processing multiple spectral (spatially coinciding) channels, it is clear that a single unique spatial alignment should be applied across all channels in a set of hyperspectral frames (provided achromatic optical performance). Independent alignment of different channels could obscure colocalization information, which is often of primary interest in HS data analysis.

Simulated HS frames were generated with a constant, high percentage (94%) area overlap between consecutive frames to approximate conditions for video-rate imaging. Zero-mean additive Gaussian noise was added to each image in every frame, in order to degrade image quality and to mimic challenging experiments that could potentially cause alignment errors. Additionally, there is a trade-off between the addition of spectral channels (increased accuracy) and computational speed [61].

The multichannel mosaicking algorithm presented by Lang *et al.* [61] applies pairwise normalized cross-correlation (NCC) as a basis for frame registration, following the previously explained algorithm of Bedard *et al.* [56]. Cross-correlation maps are calculated between consecutive image frames and the maps are normalized to an in-place autocorrelation (i.e., the theoretical maximum correlation). Correlation space then maps the probability of alignment across the spatial domain spanned by the intersection of two images being aligned, from which the location of maximum likelihood is selected as the "true" alignment location for the subsequent stitching step. We calculate the spatial cross-correlation map separately for each additional channel and average the maps in correlation space, producing a single map.

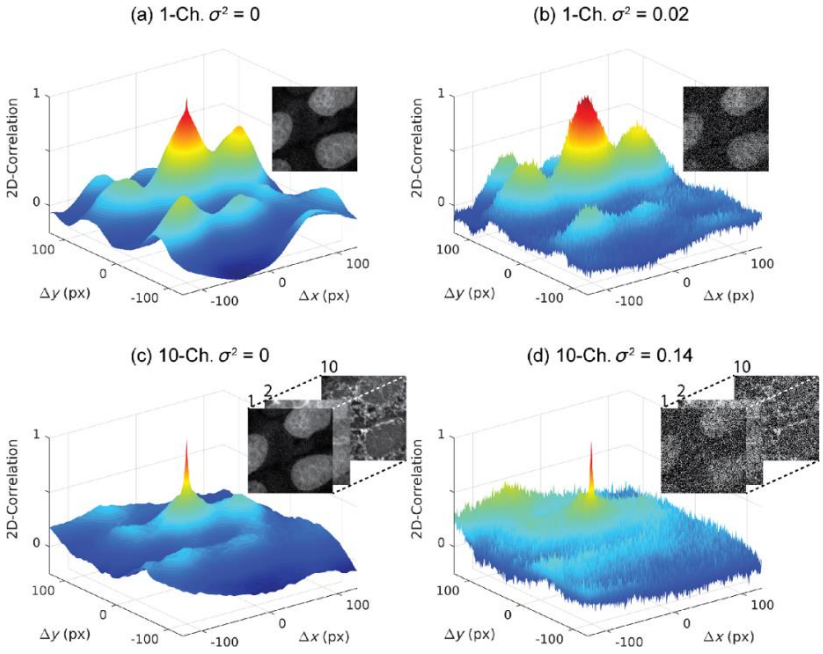

Figure 13. Exemplary cross-correlation maps demonstrate improved noise tolerance for multichannel versus single-channel micromosaicking [61].

Exemplary cross-correlation maps demonstrate improved noise tolerance for multichannel versus single-channel micromosaicking. Figure 13.b and d show that the variance in NCC space is reduced by taking the mean of multiple NCC maps, since random noise fluctuations area averaged out and reduced over several spectral channels. However, comparison of Figure 13.a and c reveal that this process also populates (sharpens) the central true peak feature while reducing the magnitudes of false peaks.

Hence, multichannel mosaicking was suggested to be more robust to noise compared to the single-channel case not only through averaging out random noise in NCC space but also because this spectral averaging apparently suppresses the false NCC peaks due to separate biological objects that share similar structural features, and therefore enhances the strength of the true peak versus false peaks.

Conclusions

In this section, and after an exhaustive study of the state of art, we realize that the number of studies applying stitching to HS images in the literature is very limited. Consequently, we hypothesize that already existing (single channel or RGB) image stitching algorithms can be adapted to process a number of simultaneous spectral channels for further HS data applications. This includes, optimization of the type of data that stitching algorithms receive (e.g. overlap between frames or number of channels per frame), as well as any further modification of the actual algorithms. Computational costs are also going to be taken into account in order to decide which parameters perform better.

Chapter 4: Materials and Methods

In this section, materials, quality assessment protocols and methods employed in this Master Thesis are introduced and further explained.

4.1. Materials

4.1.1. Image Acquisition System

The instrumentation employed in this study consists of an HS camera coupled to a conventional light microscope (Figure 14). The microscope is an Olympus BX-53 (Olympus, Tokyo, Japan). The HS camera is a Hyperspec® VNIR A-Series from HeadWall Photonics (Fitchburg, MA, USA), which is based on an imaging spectrometer coupled to a CCD (Charge-Coupled Device) sensor, the Adimec-1000m (Adimec, Eindhoven, Netherlands). This HS system works in the visual and near-infrared (VNIR) spectral range from 400 to 1000 nm with a spectral resolution of 2.8 nm, sampling 826 spectral channels and 1004 spatial pixels. The push-broom camera performs spatial scanning to acquire an HS cube with a mechanical stage (SCAN, Märzhäuser, Wetzlar, Germany) attached to the microscope, which provides accurate movement of the specimens (±3 µm accuracy). The objective lenses are from the LMPLFLN family (Olympus, Tokyo, Japan), which are optimized for infra-red (IR) observations. The light source is a 12 V, 100 W halogen lamp.

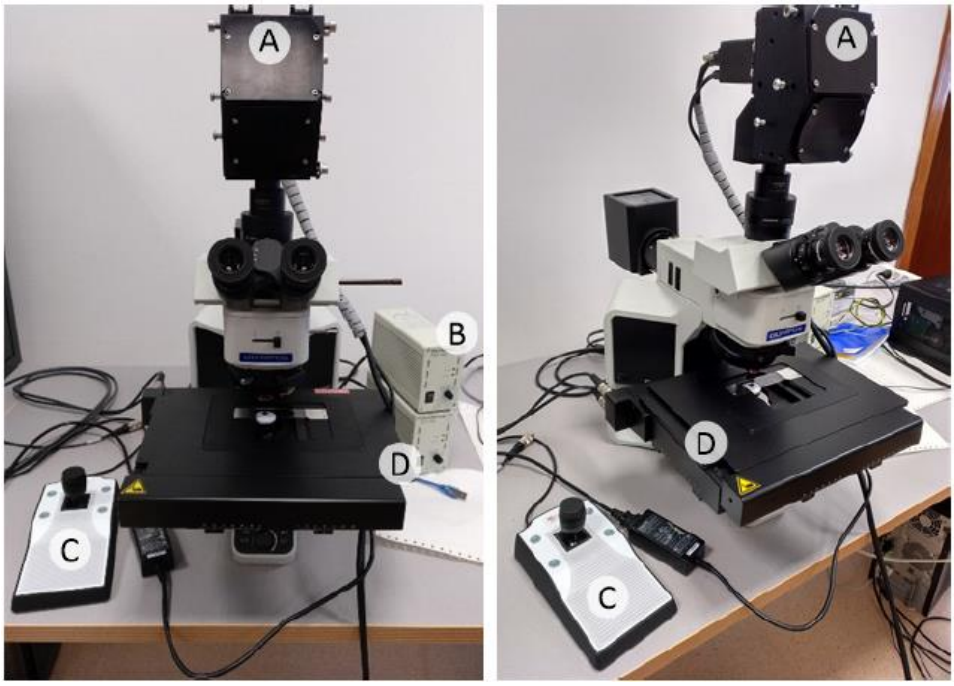

Figure 14. Microscopic HS acquisition system. a) HS camera, b) Halogen light source, c) Positioning joystick and d) XY linear stage [62].

To ensure high quality acquisitions, the methodology proposed in a previous research work to maximize the quality of HS images acquired with a push-broom microscope [63] was followed. This methodology includes the optimal speed determination of the scanning, a dynamic range configuration, an appropriate alignment, and the correct focusing procedure. Custom software for synchronizing the scanning movement and the camera acquisition was previously developed.

4.1.2. Dataset Acquisition

The specimens investigated in this research work consist of human biopsies extracted during brain tumor resection procedures. The pathological slides in this study were processed and analyzed by the Pathological Anatomy Department of the University Hospital Doctor Negrín at Las Palmas of Gran Canaria (Spain). The study protocol and consent procedures were approved by the *Comité Ético de Investigación Clínica-Comité de Ética en la Investigación (CEIC/CEI)* of the same hospital. After the resection, the samples were dehydrated and embedded in paraffin blocks. The blocks were then mounted in microtomes and sliced in 4 µm thick slices. Finally, the slices were rehydrated and stained with H&E. After routine examination of the samples, every sample was diagnosed by pathologists as GB, according to the WHO classification of tumors of the nervous system [2]. After the pathologist confirmed the GB diagnosis, macroscopic annotations of the GB locations were made on the physical glass slides using a marker-pen. Non-tumor areas are defined as areas in the pathological slide where there is no discrete presence of tumor cells. Within the areas annotated by a pathologist, regions of interest (ROI) were selected and subsequently digitized using HS instrumentation. Figure 15 shows an example of the

annotations within the pathological slide, the selection of different ROIs (shown at 5x), and the HS images (imaged at 20x) that are used in this study. Red color annotations indicate areas diagnosed as GB, while non-tumor areas were annotated in blue marker.

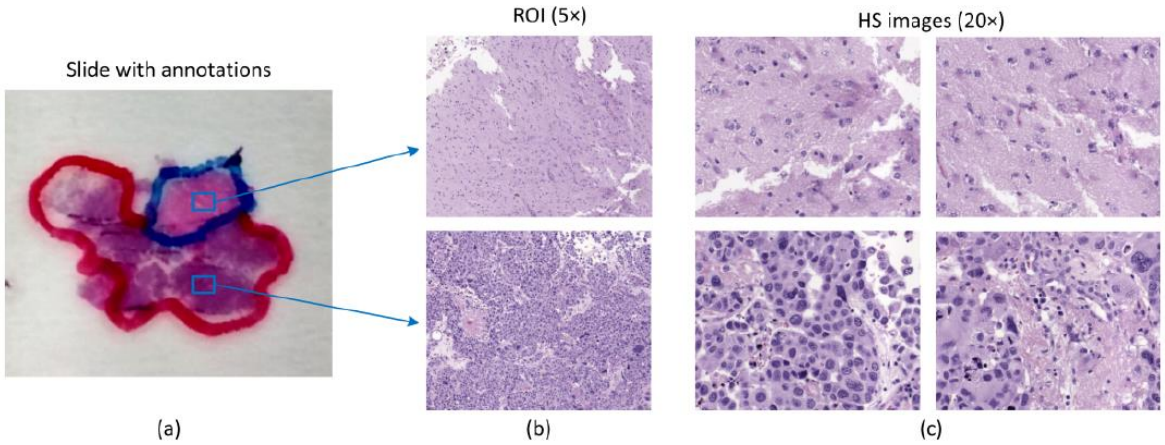

Figure 15. Pathological samples used in this study. a) Macroscopic annotations performed in pathological slides after diagnosis. Blue squares denote regions of interest (ROIs) within annotations; b) ROIs from a shown at 5x; c) of HS images used in this study for classification (imaged at 20x).

Using the aforementioned instrumentation, some of the areas highlighted by pathologists from each slide were imaged. The positioning joystick of the microscope was used to select the initial position of the first HS image within a ROI to be captured. Due to the challenges imposed by the high dimensionality of the HS images, the images employed for this Master Thesis were collected with a spatial size of 800 lines, producing HS cubes of 800 × 1004 × 826, i.e., *number of lines × number of rows × number of bands*. However, as the algorithm developed by Lang *et all.* [61] only admitted square images, cubes were cropped into 800 x 800 x 826. Furthermore, these images were scanned from histology brain tissue slides at magnification 20x, producing 2D images of size 299 x 299 µm (Figure 15.c). This magnification was chosen because it allowed the visualization of the cell morphology; hence, the classifier was able to exploit both the spatial and the spectral features of data. In this study, a total of 5 images presenting and not presenting GB were used in this Master Thesis.

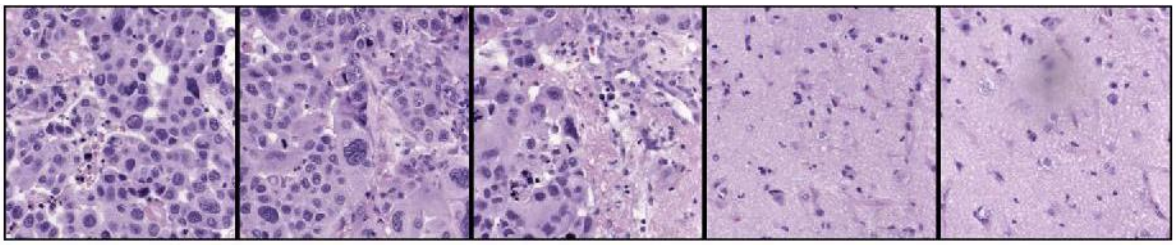

Figure 16. Database of 5 hyperspectral histological images (Represented as RGB). The 3 images at the left present GB, were the two of the right do not.

The FOV captured by a camera depend on both the lens magnification (Mi) and the sensor size of the camera (Ss), as shown in (4). The sensor size can be calculated as the product of

the pixel size of the sensor (Ps) by its number of pixels (N). Using this information, we are able to calculate the pixel size for the different magnifications. By using (4), the calculated pixel size is 0.37 µm at magnification 20x.

$$FOV = \frac{Ss}{Mi} = \frac{Ps * N}{Mi}; \quad Ps = \frac{FOV * Mi}{N} = 0.37\ \mu m/pixel \tag{4}$$

4.1.3. Processing Framework

The processing framework applied to each HS cube is composed by the following steps. First, a standard flat field correction is applied to the images. To this end, the images are transformed from radiance to normalized transmittance by using a reference image that is captured from a blank area of the pathological slide [27]. Then, due to the high correlation of spectral information between adjacent spectral bands, a reduced-band HS image is generated by averaging the neighbors' spectral bands, reducing the number of spectral bands from 826 bands to 275 and slightly reducing the white Gaussian noise. This band reduction is also beneficial for alleviating computational cost in the subsequent image processing. Moreover, the stitching algorithm was implemented in MATLAB R2019b in a Windows environment (Microsoft Windows 10) with an Intel i5-4210U 1.70 GHz CPU and 16 GB RAM.

4.2. Quality Assessment Protocol

To be able to carry out this Master Thesis, a quality assessment protocol needed to be designed for the stitched images. The problem arises when trying to measure the quality of the alignment of several small FOV images taken by the microcopy, as such large FOV image (ground truth) does not exist. We addressed this problem of quality assessment by designing an approach based on the one proposed by the Wald Protocol in 1997 [64]. Thus, instead of capturing new images and stitch them, for which we do not have ground truth, we virtually crop an image in small frames and further stitch them, being able to compare their alignment to its ground truth image from where they were firstly cropped.

Thus, as explained in Figure 17, we began degrading the FOV of a large FOV image. In this degradation process some error was incorporated in order to simulate the imperfect movements of the microscope's platform. Following, stitching algorithms were applied to the small FOV images in order to create an assembled large FOV image. Finally, the quality of the alignment was measure applying different metrics found in the state-of-the-art to the stitched images with respect to the original ones.

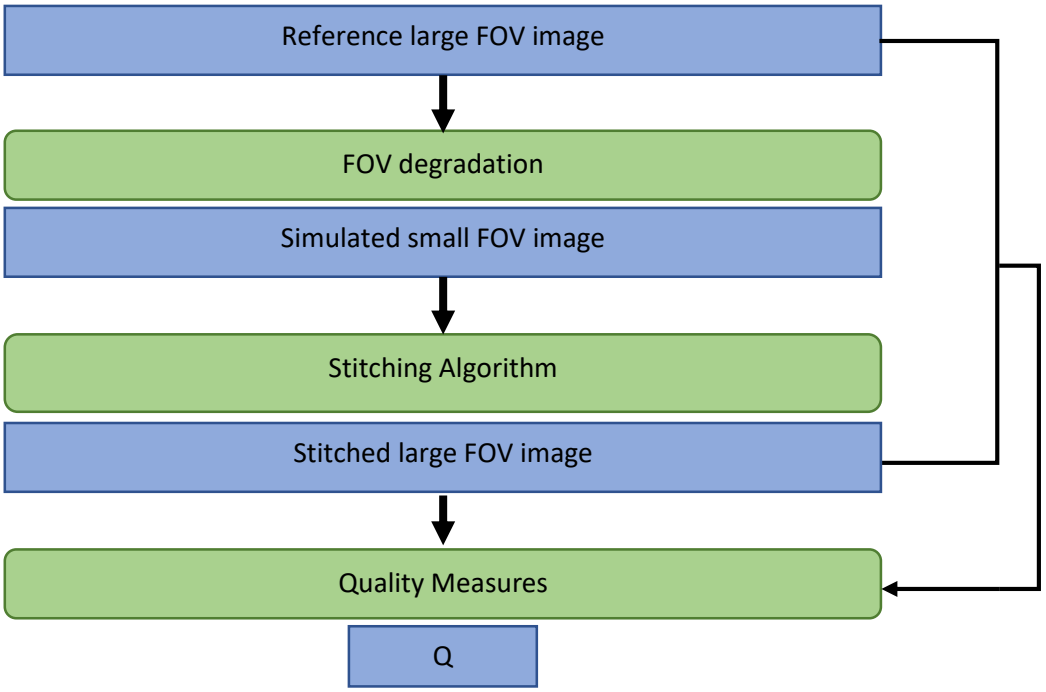

Figure 17. Block diagram of the employed Wald Protocol.

In the following sections the different processes carried out in our experiment are going to be explained more in detail.

4.2.1. Field of View Degradation (FOVD)

When working with microscopes, the FOV is highly determined by the magnification used. Pathologists, which are the ones that are going to use the assembled images, usually work in 20x to detect an event on a slide [65]. To simulate this magnification, we should apply a FOV degradation by a factor of 20. However, for simplicity of the tests, it was decided to work with a FOVD of 2. In section 4.1.2, it is shown that the size of the images employed is 299 x 299 µm, and thus the new small FOV images would have a size of 150 x 150 µm. Be aware that in this Master Thesis, although the FOV is degraded, as we are not increasing the magnification, the pixel size remains constant and, as calculated in section 4.1.2, it is 0.37 µm. In real life, if we increase by a factor of 2 the FOV (magnify the image 2x), the pixel size would be reduced by the same factor.

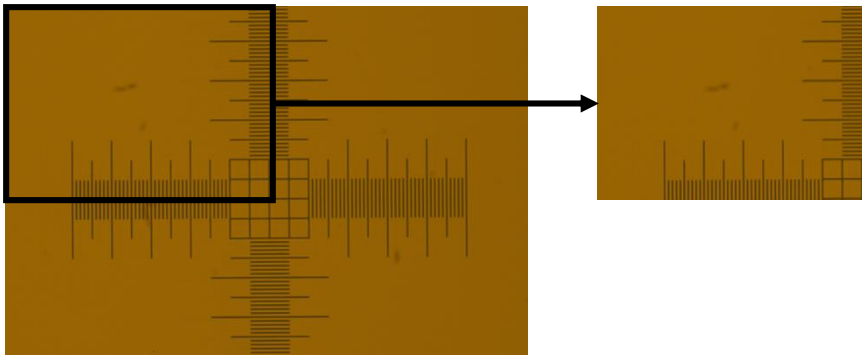

Figure 18. FOVD of 2 divide the FOV by 2.

Another variable to take into account was the overlap between the small FOV images. The overlap that is going to be used in this project is defined as the percentage that one image $i+1$ shares with its predecessor, i. As shown in (5), the value of the overlap depends on the FOV degradation and the number of small FOV images (Nsi) that are cropped in each direction. In this way, it is possible to have different overlaps for X and Y axis. However, for simplicity of the test we are going to set the same overlap for both axes.

$$Overlap = \frac{Nsi - FOVD}{Nsi - 1} \tag{5}$$

In the same way, the number of small FOV images is defined as equation (6).

$$Nsi = \frac{overlap - FOVD}{overlap - 1} \tag{6}$$

As in this Master Thesis the FOVD is set to 2, the overlap follows the plot shown in Figure 19. Equation (5) has an asymptote in $overlap = 1$. For this reason, in our empirical tests we decided to stop at $overlap = 0.92$ ($Nsi = 13$), where the graph reach a plateau.

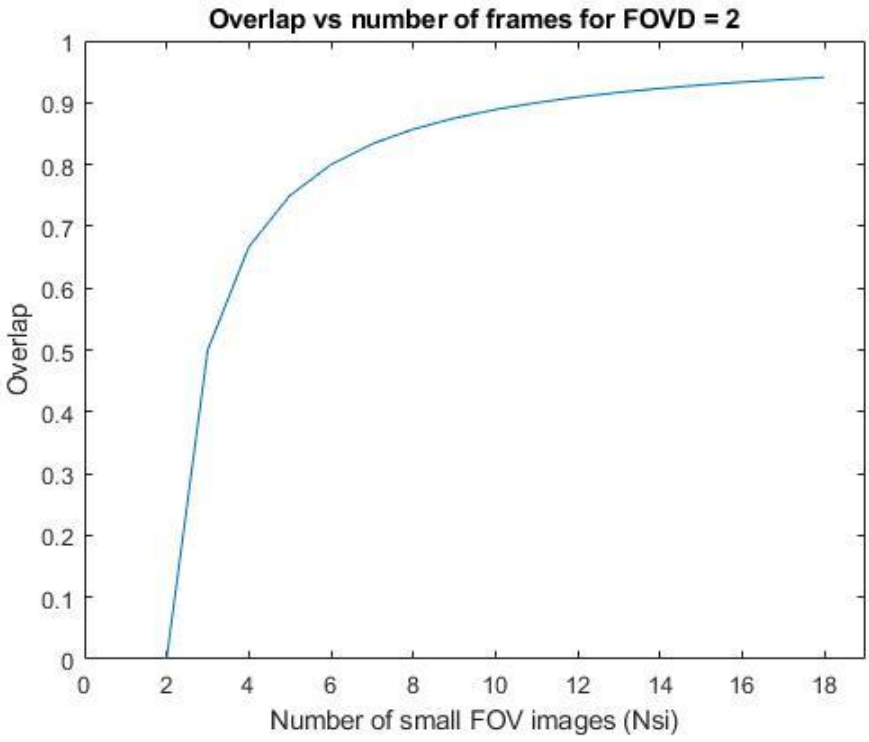

Figure 19. Overlap versus number of small FOV images ($FOVD = 2$).

For example, in Figure 20 there are shown two sets of small FOV images with different overlaps ($FOVD = 2$).

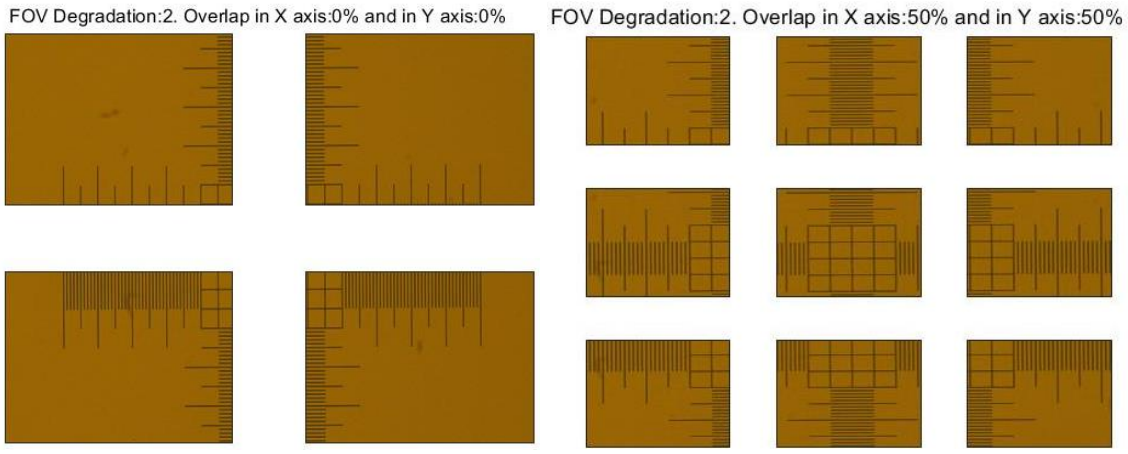

Figure 20. Example of different overlap images.

However, such a perfect degradation cannot be achieved in real life. The most common inaccuracies caused when taking pictures for stitching algorithms are rotational, scaling and translational errors [66]. When working with the platform of our microscope, small rotational errors caused by vibration of the platform or little scaling errors due to different heights within the same slide, can be neglected. However, and as we saw in section 4.1.1, we have to deal with 3 µm translational error. The maximum translational error (in pixels) that the platform can cause at 20x was calculated in (7).

$$Error\ (pixels) = \frac{Error}{Pixel\ Size} = \frac{3\mu m}{0.37\ \frac{\mu m}{pixel}} = 8\ pixels \tag{7}$$

Thus, when degrading the FOV, errors were simulated by translating the small FOV images a random number of pixels within the range -8 to 8. To be able to do that, the image was first added an 8-pixel frame around itself.

Furthermore, and as seen in (8), we can calculate the maximum error percentage taking into account the error in pixels previously calculated and the size of the FOV. Since the error is the same for both axes, and we are working with a square cube, error would be the same for both axes.

$$Error\ (\%) = \frac{Error}{FOV} * 100\ = \frac{3}{375} * 100 = 0.8\% \tag{8}$$

The last variable that we should take into account is the number of frames (Nf) taken. For a constant FOVD and overlap, the number of frames taken goes from the minimum number of small FOV images possible, that is the same as the FOVD, to the number of small FOV images necessary to reconstruct the original image based on the overlap (9).

$$FOVD \leq Nf\ \leq \frac{overlap - FOVD}{overlap - 1} \tag{9}$$

In Table 1 it is shown the configuration for different number of frames taken and their corresponding overlaps. For the interpretation of this Table, it has to be taken into account that the diagonal represents the Nsi necessary to reconstruct the whole image.

Table 1. Configuration for different number of frames taken and their corresponding overlaps (FOVD = 2)

overlap \ Nf	0	0.5	0.67	0.75	0.8	0.83	0.86	0.88	0.89	0.9	0.91	0.92
2	X	X	X	X	X	X	X	X	X	X	X	X
3		X	X	X	X	X	X	X	X	X	X	X
4			X	X	X	X	X	X	X	X	X	X
5				X	X	X	X	X	X	X	X	X
6					X	X	X	X	X	X	X	X
7						X	X	X	X	X	X	X
8							X	X	X	X	X	X
9								X	X	X	X	X
10									X	X	X	X
11										X	X	X
12											X	X
13												X

Thus, the less Nf we take, the less reconstructed the original image would be.

$$\frac{reconstructed\ FOV}{original\ FOV} * 100 = \frac{(Nf - (Nf - 1) * overlap)}{(Nsi - (Nsi - 1) * overlap)} * 100 \qquad (10)$$

For example, in Figure 21 are shown two configurations with equal FOVD and overlap, but different number of frames taken. Specifically, $FOVD = 2$ and $overlap = 50\%$, thus we are in column 2 of Table 1 and the number of frames taken that we can choose are 2 or 3. As 3 is the value in the diagonal, it is the one that would reconstruct the original image (Figure 21.a). It can be proved using (6) that $0.5 - 2/0.5 - 1 = 3$. However, if we choose 2 frames to reconstruct the original image (Figure 21.b), only 75% of it would be reconstructed (from (10): $2 - 0.5/3 - 1 = 0.75$).

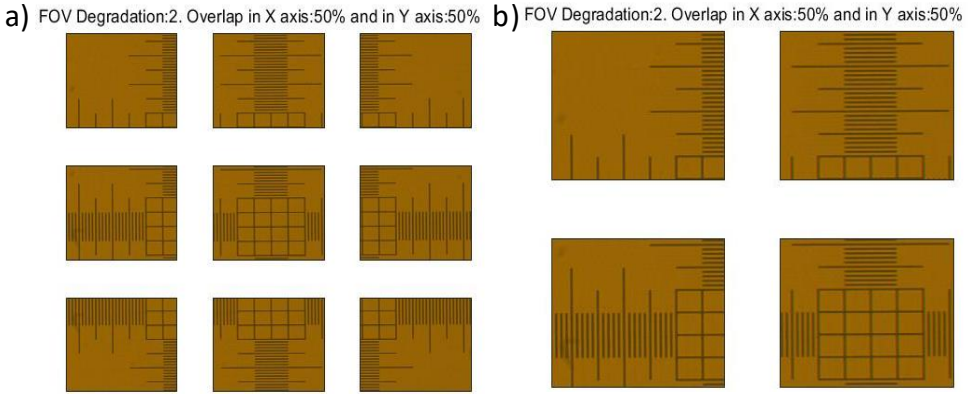

Figure 21. Same FOVD degradation and overlap was set for both images. a) The area reconstructed is 100% the original image and b) The area reconstructed is 75% the original image.

4.2.2. Stitching Algorithm

For this Master Thesis, we decided to employ two different stitching methods, that we named manual and automatic stitching. The manual stitched consisted in just mosaicking the images one next to each other, without any kind of further processing. However, for the automatic stitching a more complex algorithm, developed by Ryan T. Lang *et all.* [61], was used.

For the automatic stitching, cross-correlation maps are calculated between consecutive image frames. To do so, a serpentine pattern (Figure 12) was followed, where $i + 1$ indicates the contiguous vertical frame of i. Then, the maps are normalized to an in-place autocorrelation (i.e., the theoretical maximum correlation). Correlation space then maps the probability of alignment across the spatial domain spanned by the intersection of two images being aligned, from which the location of maximum likelihood is selected as the "true" alignment location for the subsequent stitching step. We calculate the spatial cross-correlation map separately for each additional channel and average the maps in correlation space, producing a single map. The algorithm imposes some limitations, such as a limited number of spectral bands (10) and the aspect ratio of the image to be one (images should be square shape).

4.2.3. Quality Metrics

Image quality evaluation methods can be subdivided into objective and subjective methods [67]. Subjective methods are based on human judgment and operate without reference to explicit criteria. However, determining which method provides a better-quality image could vary from person to person. For this reason, it is also necessary to establish quantitative measures to quantify the effects of image stitching algorithms on image quality. Objective methods are based on comparisons using explicit numerical criteria, and references are possible such as the ground truth we are using for this project. The different image quality metrics employed in this Master Thesis will be explained below.

Root Mean Square Error (RMSE)

The root mean square error can be used as an evaluation criterion of the stitching method. The RMSE between each stitched image band and the corresponding reference band can be computed as a measure of spectral fidelity. Specifically, it measures the amount of change per pixel due to the processing of stitching [68]. Given a reference image f and a test image g, both of size MxN, the RMSE is given by (11).

$$RMSE = \sqrt{\frac{1}{MNP}\sum_{0}^{P-1}\sum_{0}^{M-1}\sum_{0}^{N-1}\|f(i,j) - g(i,j)\|^2} \tag{11}$$

Thus, the lower the RMSE, the higher stitched image quality.

Although the correlation coefficient (CC) can be also used as a metric for the similarity of two images, during Pradham research [68], it was found that the RMSE has a higher resolution compared to the correlation coefficient. And thus, this metric is not going to be taken into account for this experiment.

Peak Signal to Noise Ratio (PSNR)

The term peak signal-to-noise ratio (PSNR) is an expression for the ratio between the maximum possible value of a signal and the power of distorting noise that affects the quality of its representation (12). Because many signals have a very wide dynamic range, the PSNR is usually expressed in terms of the logarithmic decibel scale.

The peak signal-to-noise ratio can be also used to compare image assembly quality. As for the RMSE, images f and g are going to be evaluated by the PSNR which is defined by (12).

$$PSNR = 20\ \log_{10}\left(\frac{MAX_f}{\sqrt{MSE}}\right);\ \ where\ MSE = \frac{1}{MNP}\sum_{0}^{P-1}\sum_{0}^{M-1}\sum_{0}^{N-1}\|f(i,j) - g(i,j)\|^2 \qquad (12)$$

The mean square error (MSE) represents the cumulative squared error between the stitched and the original image, whereas PSNR represents a measure of the peak error. The PSNR value approaches infinity as the MSE approaches zero; this shows that a higher PSNR value provides a higher image quality [69].

The main limitation of this metric is that it relies strictly on numeric comparison and does not actually take into account any level of biological factors of the human vision system such as the structural similarity index (SSIM).

Structural Similarity Index (SSIM)

The SSIM is a well-known quality metric used to measure the similarity between two images. It was proposed by Wang et al. [70], and is considered to be correlated with the quality perception of the human visual system (HVS). Instead of using traditional error summation methods, the SSIM is designed by modeling any image distortion as a combination of three factors that are loss of correlation, luminance distortion and contrast distortion. As for the PSNR, given a reference image f and a test image g, the SSIM is defined in (13).

$$SSIM\ (f,g) = l(f,g)\ c(f,g)\ s(f,g);\quad where\ \begin{Bmatrix} l(f,g) = \dfrac{2\mu_f\mu_g + C_1}{\mu_f^2 + \mu_g^2 + C_1} \\ c(f,g) = \dfrac{2\sigma_f\sigma_g + C_2}{\sigma_f^2 + \sigma_g^2 + C_2} \\ s(f,g) = \dfrac{\sigma_{fg} + C_3}{\sigma_f\sigma_g + C_3} \end{Bmatrix} \qquad (13)$$

The first term in (13) is the luminance comparison function which measures the closeness of the two images' mean luminance (μ_f and μ_g). This factor is maximal and equal to 1 only if $\mu_f = \mu_g$. The second term is the contrast comparison function which measures the closeness of the contrast of the two images. Here the contrast is measured by the standard deviation $\sigma_f$and σ_g. This term is maximal and equal to 1 only if $\sigma_f = \sigma_g$. The third term is the structure comparison function which measures the correlation coefficient between the two images f and g. Note σ_{fg} is the covariance between f and g. The positive constants C_1, C_2 and C_3 are used to avoid a null denominator. The positive values of the SSIM index are in the range [0,1]. A value of 0 means no correlation between images, and 1 means that both images are equal [69].

4.3. Methods

In this section the methodology that was followed during the development of this Master Thesis is explained.

4.3.1. Manual Stitching

First of all, the manual stitching process was carried out. As for this process the overlap only could be 0%, then the only possible number of frames taken was 2, the same number of small FOV images ($N_{si} = N_f = 2$). Thus, the reconstructed image size was 100% of the original one.

4.3.2. Automatic Stitching

However, the automatic stitching process is more complex. The goal here was to find the minimum overlap necessary between contiguous images as well as the minimum combination of bands that provide the maximum performance in the final stitched image. To achieve it, we designed a two-steps methodology (

Figure 22). First of all, from Table 1, the best overlap and N_f configuration was going to be selected. And afterwards, single band stitching was going be performed and the best stitching mosaics would show which wavelength perform better for this type of images.

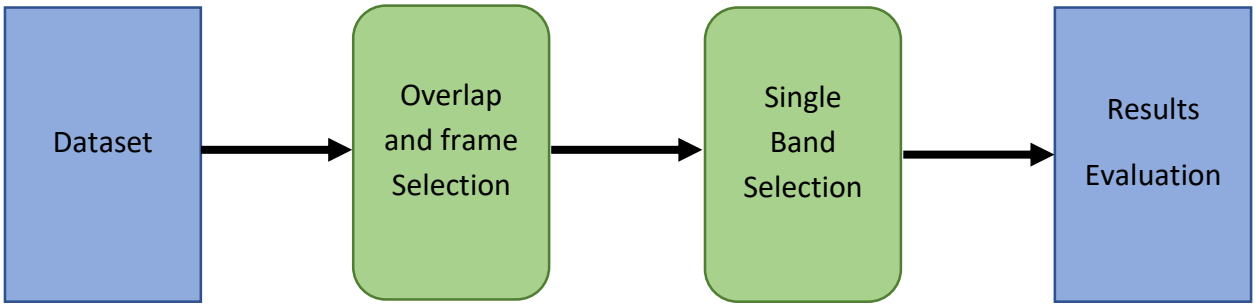

Figure 22. Flow diagram of the methodology employed.

Overlap and Frame Selection

In this first step, the goal was to find the minimum overlap that produced the most accurate stitched image, while the maximum number of frames to reconstruct the original image. In other words, the closest to the right and the diagonal in Table 1.

We tested a wide range of different overlaps to see their performance**¡Error! No se encuentra el origen de la referencia.**. The maximum overlap that we used was the one for which the function reached the plateau, 92%. The minimum overlap possible is given by the translational error percentage, in this case 0.8%.

$$0.8\% \leq Overlap \leq 92\% \tag{14}$$

If substituting this values into (6), and taking into account that N_{si} can just take natural values, we have that the number of small FOV images goes as in (15).

$$3 \leq Nsi \leq 13 \tag{15}$$

In this way, we are going to obtain 3D plots were, x and y axes correspond to overlap and frames, respectively, while z axis is the value of each single figure of metric.

Furthermore, although, the number of bands of the image was no subject of study in this first step, we tested these parameters into different image channel configurations to see the behavior of the algorithm (a RGB image, a 10-band multispectral image and a grayscale image).

As a neutral image, we used an artificial RGB image extracted from the original HS image (Figure 23). For this process we tried to imitate as much as possible the human eye spectral response. Thus, we applied the normal probability density function for the three different RGB bands. Based on Figure 23, the mean band selected for the blue channel was 470 nm with standard deviation (std) equal to 0.04, for the green channel, 560 nm with a std of 0.06 and for the red channel 590 nm with a std of 0.08.

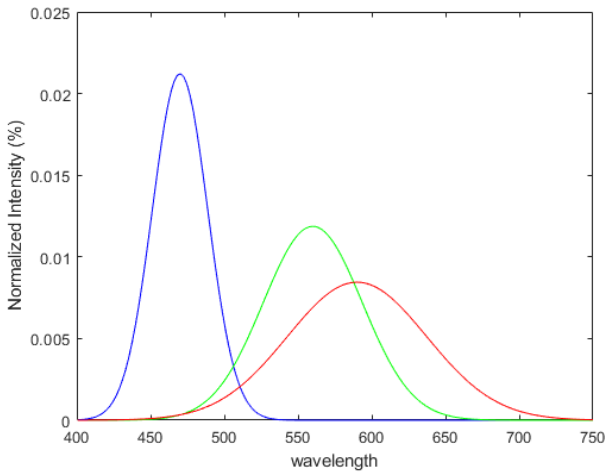

Figure 23. Human eye spectral response to light [71].

Then, to test how the algorithm respond to more bands, a 10-band image was used. These 10-band images were generated from the 275-band cube, extracting 10 equidistant distributed bands (Figure 24).

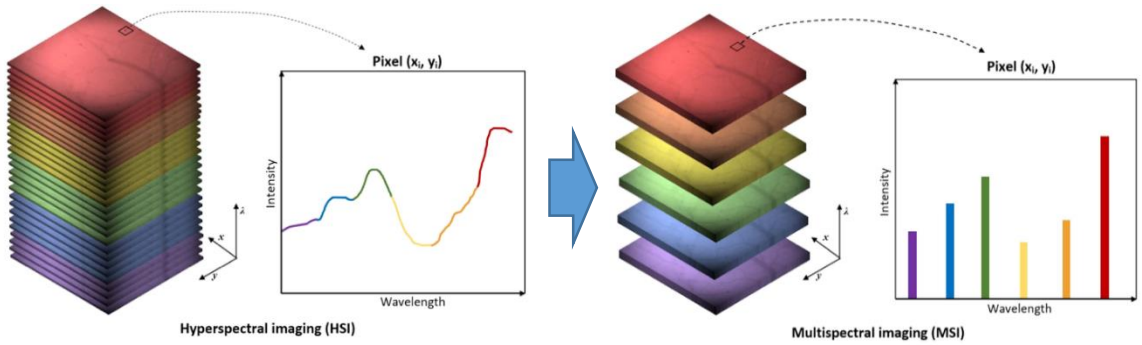

Figure 24. HSI bands to 10 Multispectral imaging bands [72].

And finally, to test how the algorithm respond to few bands, a grayscale image was employed. This image was generated from the mean value of each pixel through the 275 bands of the HS cube.

Finally, the quality of the stitched image was measure in these three different types of images for all the configurations of overlaps and all their possible number of frames. The optimum overlap and frames were selected from these experiments.

Band Selection

In this second step, the goal was to find the single band or the best band subset that produced the best stitching. This selection will bring benefits such as smaller processing time or resources employed by the selected stitching algorithm.

Band reduction denotes the group of techniques that reduce high dimensional data to a smaller set of components. Reduction can be performed by either identifying bands from the original subset (selection), or by employing several transforms that produce new features (extraction) [73]. As we are doing a prove of concept, a selection method was employed. Thus, for the second step, the quality assessment protocol was performed over every single band. Each channel in the 275-band cube, was degraded into smaller frames, then stitched and finally measured. Finally, the band and band range providing the best stitched image accuracy was selected.

Final Image Selection

In this third and last step, the goal was to determine how different channel combinations behaved. Firstly, it was made a selection of the 3 wavelengths which produced the most accurate stitching results, and a cube was created from them. Additionally, a new grayscale image was created from as the average of such 3 selected bands. Furthermore, a selection of 10 bands was made, also within the range of better performing wavelengths, and a grayscale image was also created from the 10 selected bands.

Conclusions

In this section the materials needed to carry out this project, the image acquisition system as well as the histology images dataset have been described. It was also explained the quality protocol, based on the Wald Protocol, that is going to be followed. Finally, every step of the methodology was defined. First, a manual stitching is going to be performed as a baseline method. Then the algorithm of Lang *et all.* [61] is going to be employed in this work. Optimal selection of overlap and frames are going to be found, as well as the wavelength that offer the most accurate mosaic. Finally, some channel combination images are going to be created, from the more suitable wavelengths in this particular application, in order to evaluate their stitching accuracy.

Chapter 5: Results

In this section, the results of the methods described before will be shown for further analysis and discussion.

5.1. Manual Stitching

Manual stitching consisted in mosaicking the images one next to each other, without further processing. Note that, as the pictures are being assembled one next to another, 0% overlap is needed. In this way the number of frames needed to reconstruct the original image is equal to the field of view degradation ($FOVD = 2$ in this case). As we can see in Table 2, metrics for this kind of stitching algorithms are not bad.

Table 2. Results obtained for the Manual Stitching approach.

	RGB	10 bands	Grayscale
RMSE	0.10 ± 0.02	0.08 ± 0.01	0.07 ± 0.01
PSNR (dB)	19.88 ± 1.70	22.02 ± 0.89	23.54 ±0.62
SSIM	0.83 ± 0.03	0.89 ± 0.02	0.84 ± 0.04

Nevertheless, as we can see in an example of this stitching process (Figure 25), although the image is equal to the original in the majority of the mosaic, it is really inaccurate in the areas where the images are being assembled. For example, if stitching two frames, one next to each other, most of the image would be the same as the original one, since it is contained in the small FOV image. However, the right border of the left image will no coincide with the left border of the right image because of the platform translational error, and there is where errors arises.

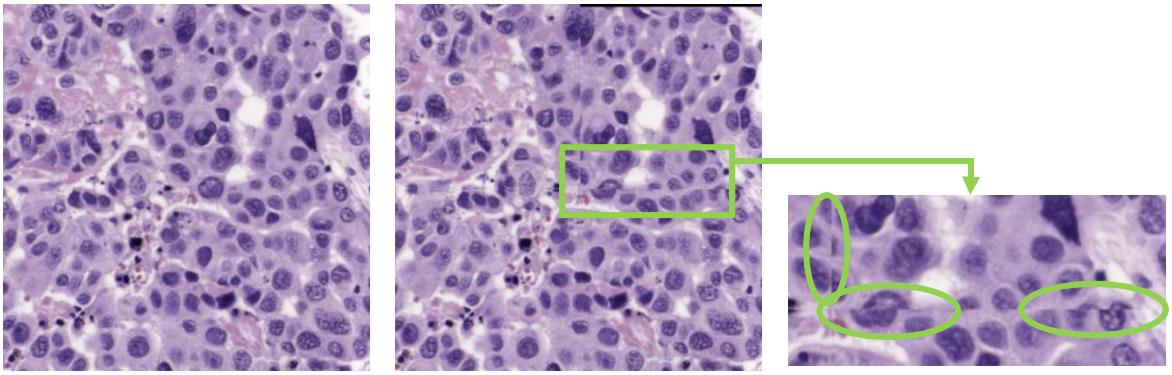

Figure 25. Example result of a manual stitching of a brain histology image.

5.2. Automatic Stitching

After the manual stitching was conducted, we proceeded to employ Lang *et al.* [61] algorithm. As described in section 4.2.2, a test bench was employed to be able to test the different parameters involved in the stitching process.

5.2.1. Overlap and Frame Selection

Firstly, we tested the overlap selected and the frames employed, at the same time. This meaning that for each image we have, it was tested all the possible frames for a certain overlap and all the overlaps between 50% and 92%. We can see an example of a chart obtained for SSIM in Figure 26.

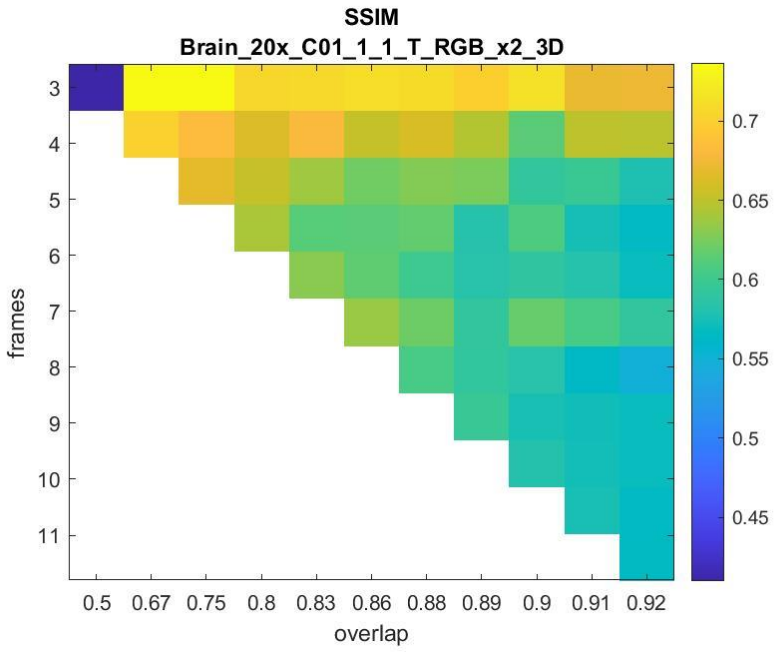

Figure 26. SSIM result of image 'Brain_20x_C01_1_1_T' for all overlaps an its corresponding frames. Colorbar indicate the SSIM value for a certain pair of parameters combination.

This procedure was repeated for 5 different brain histology images in the form of RGB, 10 bands and Grayscale. Then, for each image it was found the overlap and frames for which each image had the minimum value for RMSE and the maximum values for PSNR and SSIM. After that, the means for overlap, frames and metric were calculated and the parameters are shown in Table 3.

Table 3. Overlap and Frames for 5 brain histology images.

		5 Brain Histology Images		
		RGB	**10 bands**	**Grayscale**
RMSE	**Mean Min Value**	0.13 ± 0.01	0.11 ± 0.00	0.19 ± 0.01
	Overlap	0.67 ± 0.00	0.77 ± 0.13	0.72 ± 0.11
	Frames	**3.00 ± 0.00**	**3.00 ± 0.00**	**3.00 ± 0.00**
PSNR (dB)	**Mean Max Value**	17.33 ± 0.93	18.78 ± 0.25	14.48 ± 0.52
	Overlap	0.67 ± 0.00	0.72 ± 0.11	0.72 ± 0.11
	Frames	**3.00 ± 0.00**	**3.40 ± 0.55**	**3.00 ± 0.00**
SSIM	**Mean Max Value**	0.78 ± 0.05	0.80 ± 0.05	0.43 ± 0.04
	Overlap	0.76 ± 0.12	0.80 ± 0.12	0.80 ± 0.12
	Frames	**3.00 ± 0.00**	**3.40 ± 0.55**	**3.40 ± 0.55**

Results show some consistency with Lang *et al.* [61] conclusions, where multichannel correlation demonstrated to improve the noise tolerance of HS microimage mosaicking versus single channel correlation. We can observe in Table 3 how the quantitative metric results are better for 10-band cube, then for RGB images and finally for Grayscale ones. Moreover, the mean overlap between frames is considerably smaller than the one that Lang *et al.* [61] used in their experiments, 94%. Thus, we can state that microscopy slides do not need as much overlap between frames as microendoscope video frames.

As for the frame values, it is clearly shown that the most repeated frame number was 3, and thus we selected this value. However, the optimal overlap number is not clear. To select the overlap, it was chosen the one which better reconstructed the original image from the selected frames. Note that to reconstruct the original image from 3 frames will require a 50% overlap, but according to the results this overlap does not produce high quality mosaics. The next possible overlap would be 67%, and this value was selected since it reconstructs almost the whole original image (83% as seen in equation (16)).

$$\frac{reconstructed\ area}{original\ area} = \frac{3 - 2 * 0.67}{4 - 3 * 0.67} = 83\% \qquad (16)$$

A more graphical representation of this situation is shown in Figure 27, where the figure of the left is the original image, and the one in the right is the reconstructed one from 3 frames and 67% overlap.

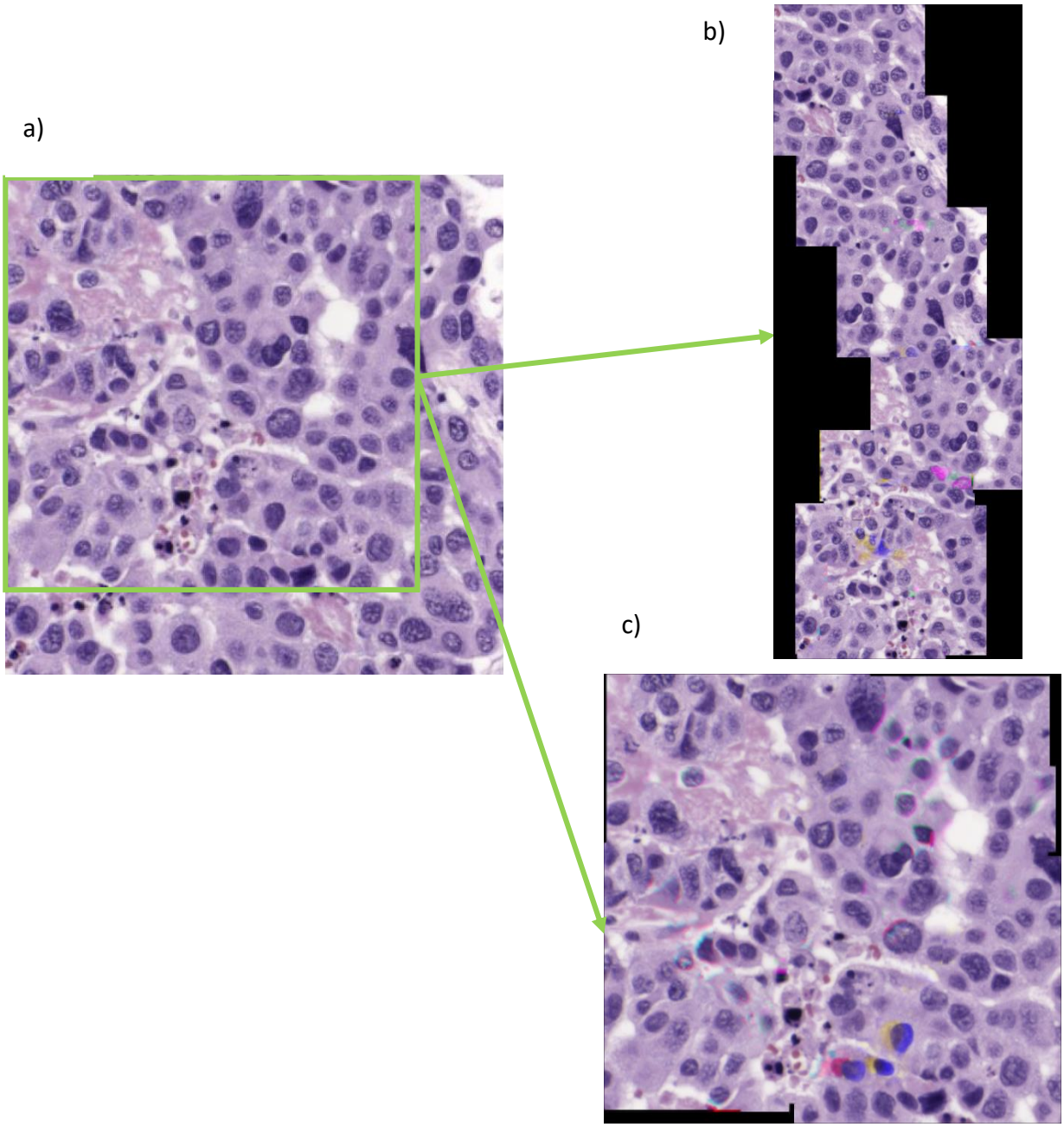

Figure 27. Brain histology images a) Original image and b) Reconstructed 100% of the original image from 3 frames at 50% overlap and c) Reconstructed 83% of the original image from 3 frames at 67% overlap.

To test the repeatability of the tests, we did the same procedure over 4 breast histology images and the results are shown in Table 4.

Table 4. Metric results, overlap and frames for 4 breast histology images.

		4 Breast Histology Images		
		RGB	**10 bands**	**Grayscale**
RMSE	**Mean Min Value**	0.11 ± 0.01	0.16 ± 0.01	0.12 ± 0.01
	Overlap	0.73 ± 0.12	0.79 ± 0.14	0.67 ± 0.00
	Frames	**3.00 ± 0.00**	**3.25 ± 0.50**	**3.25 ± 0.50**
PSNR (dB)	**Mean Max Value**	19.33 ± 0.61	16.05 ± 0.55	18.66 ± 0.58
	Overlap	0.73 ± 0.12	0.79 ± 0.14	0.67 ± 0.00
	Frames	**3.00 ± 0.00**	**3.25 ± 0.50**	**3.25 ± 0.50**
SSIM	**Mean Max Value**	0.96 ± 0.00	0.61 ± 0.03	0.74 ± 0.04
	Overlap	0.79 ± 0.74	0.84 ± 0.12	0.73 ± 0.04
	Frames	**3.00 ± 0.00**	**3.00 ± 0.00**	**3.25 ± 0.05**

For this kind of images, it is not as evident that multichannel correlation improves stitching images, since the best metrics are not always found for the 10 band images, nor the worst ones for the Grayscale frames. However, we are only testing 4 images as a proof of concept, and thus, their results may not be quite reliable. More images should be tested in order to validate the methodology and the results. Additionally, the most repeated frame is again 3, and thus, the overlap value selected is 67%.

5.2.2. Band Selection

Once the frames were selected to be 3 and the overlap 67%, and since there was no clear better stitching metrics from one kind of image to another, we proceeded to test each band individually. The motivation to realize this kind of test comes from the own nature of the images, since histology slides usually have similar color characteristics, it was hypothesized that an optimal subset of wavelengths could be selected to produce accurate mosaics. Moreover, this selection would bring benefits such as smaller processing time or resources employed by the selected stitching algorithm.

To do that, we employed the pre-processed images containing 275 bands and performed the Wald Protocol (Figure 17) to each band independently. That is, taking a single band image and crop it into smaller frames. Then stitch together the small frames and finally compare the resulting mosaic with the original single band image. This process was repeated for the 275 bands of each of the 5 brain histology images. Then, for each band the mean of the 5 images metric value was performed , as shown in Figure 28 and Figure 29.

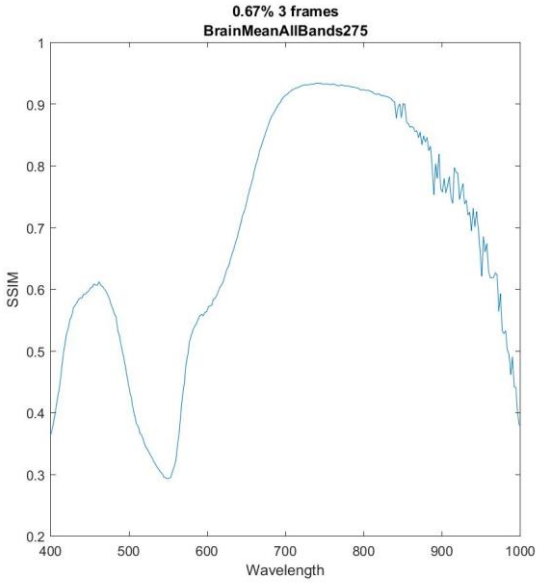

Figure 28. Plot of mean SSIM result vs wavelength for 5 Brain Histology images (275 bands) using 67% of overlap and 3 frames.

As expected, the RMSE and PSNR results have similar curves, but one is the inverse of the other one.

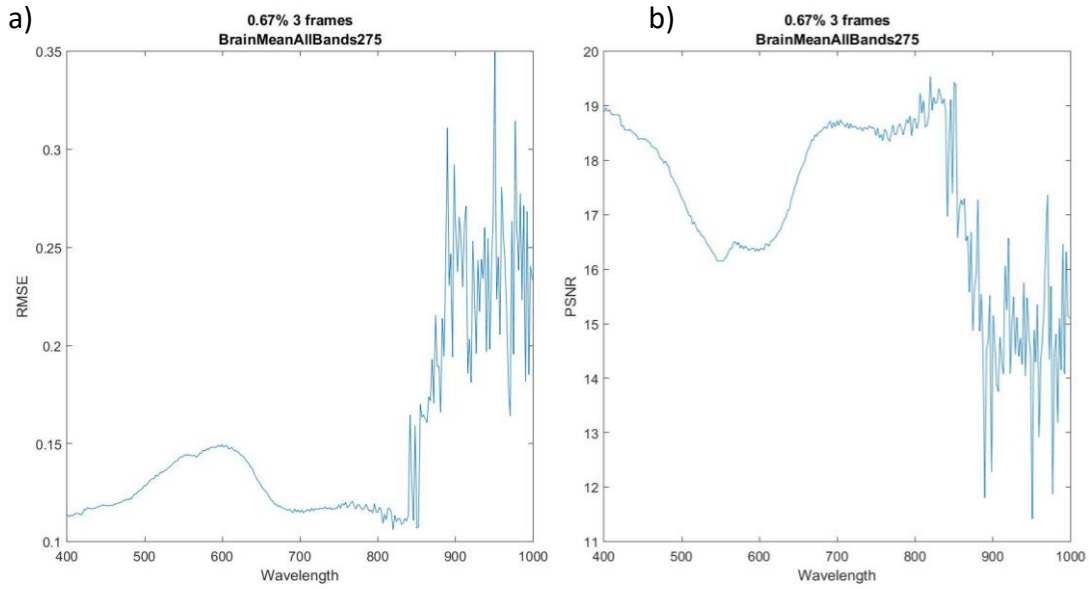

Figure 29. Plots of mean values for 5 Brain Histology images (275 bands) using 67% of overlap and 3 frames. a) Plot of mean RMSE vs wavelength and b) Plot of mean PSNR vs wavelength.

However, in these results, noise can be observed from wavelength 764,997 nm onwards, leading to fatal errors in the mosaics. Thus, it was decided to remove some of the initial and last bands from the HS image, obtaining a cube of 159 bands instead of 275. Thus, the graph for the SSIM result is shown in Figure 30 and the ones for the RMSE and PSNR results in Figure 31.

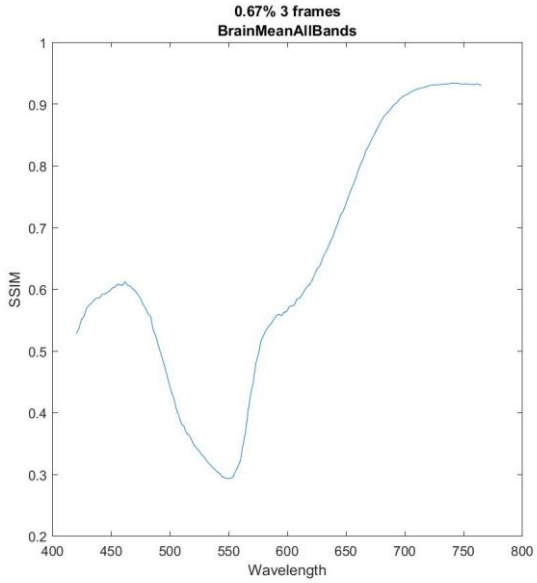

Figure 30. Plot of mean SSIM results vs wavelength for 5 Brain Histology images (159 bands) using 67% of overlap and 3 frames.

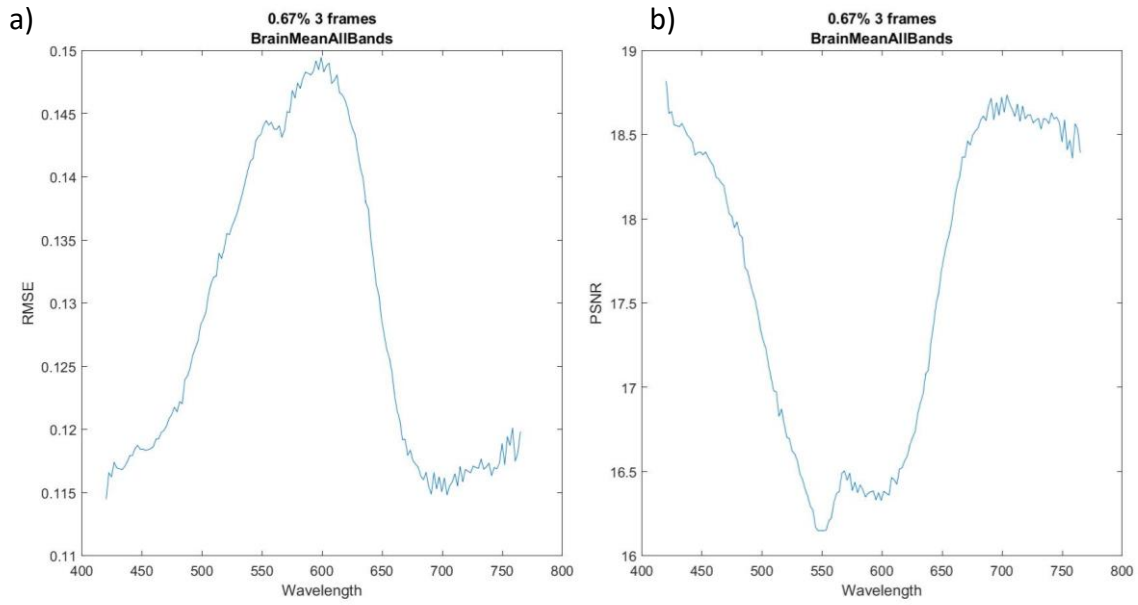

Figure 31. Graphs of mean values for 5 Brain Histology images (159 bands) using 67% of overlap and 3 frames a) Plot of mean RMSE vs wavelength and b) Plot of mean PSNR vs wavelength.

Previous figures demonstrate that there is a dependency between wavelength and metric quality. Thus, some wavelengths show clear better results than other ones, providing minimum RMSE and maximum PSNR and SSIM values. They are presented in further detail in Table 5.

Table 5. Average single band best metric results for the 5 Brain Histology Images

		159 Bands Brain Cube
RMSE	**Mean Min Value**	0.1148
	Wavelength (nm)	703.8810
PSNR (dB)	**Mean Max Value**	18.7355
	Wavelength (nm)	703.8810
SSIM	**Mean Max Value**	0.9340
	Wavelength (nm)	738.8050

From the graphs and table, we can extract that the most accurate stitching results would be given from bands in the range of wavelength 650 to 750 nm. Furthermore, Figure 30 shows a peak in the red region (~635-700 nm) and a smaller one in the blue and violet region (~400-490 nm), but a valley in the green region (~520-560 nm). We have hypothesized that this behavior is due to the nature of the histology images, as they were stained with H&E (Hematoxylin and Eosin), where hematoxylin stains cell nuclei blue, and eosin stains the extracellular matrix and cytoplasm pink [13]. Therefore, no green components were present in the slide, nor in the HS cube. Thus, when performing the stitching process on the green wavelengths, no reference points were available for the registration of the frames.

As in the previous step, to check the repeatability of these tests in different histological images, we repeated the same procedure with the 4 breast histology images. The graphs obtained are shown in Figure 32 and Figure 33.

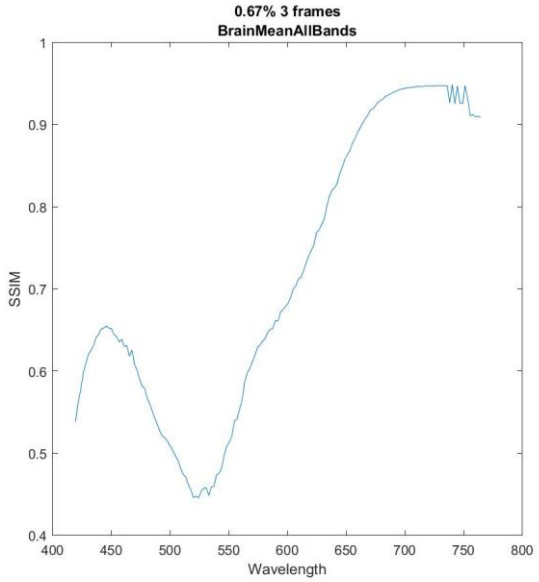

Figure 32. Plot of mean SSIM vs wavelength for 4 Breast Histology images (159 bands) using 67% of overlap and 3 frames.

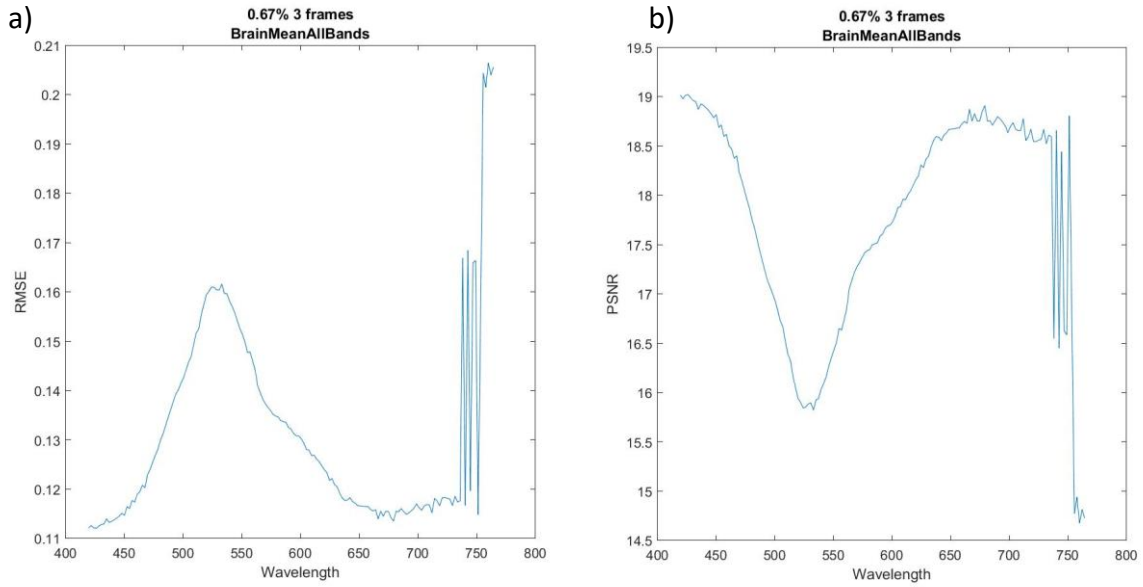

Figure 33. Graphs of mean values for 4 Breast Histology images (159 bands) using 67% of overlap and 3 frames a) Plot of mean RMSE vs wavelength and b) Plot of mean PSNR vs wavelength.

We can observe in Figure 32 the peaks in the red, blue and violet regions, and de valley in the green one. These results are consistent with brain histology images, as breast histology images were also stained with H&E. Moreover, the following Table 6 shows the minimum RMSE and the maximum PSNR and SSIM values also shown in previous charts.

Table 6. Average single band best metric results for the 4 Breast Histology Images

		159 Bands Breast Cube
RMSE	Mean Min Value	0.1121
	Wavelength (nm)	425.9470
PSNR (dB)	Mean Max Value	19.0209
	Wavelength (nm)	425.9470
SSIM	Mean Max Value	0.9481
	Wavelength (nm)	740.2600

From the previous Table 6, we can observe that SSIM measure is in the range of 650 – 750 nm, as for the brain histology images, but RMSE and PSNR best quality measure are not in this range. However, they are in the range of the blue and violet region (~400-490 nm), which are also present colors in this type of images. Moreover, although for RMSE and PSNR, minimum and maximum values, respectively, are found in wavelength 425 nm, values in the range 650 – 750 nm are also really close to them, as we can see in Figure 33

5.2.3. Final Image Selection

Once the frame, overlap and wavelength range were selected, we tested several image configurations to evaluate their behavior. Firstly, from the results from the independent band stitching, we selected 10 and 3 bands with SSIM values higher than 0.75 and wavelengths between 650 and 750 nm (Table 7 and Table 9, respectively).

Table 7. 10 bands selection with it correspondent SSIM values for Brain Cubes

5 Brain Histology Images	
Wavelength (nm)	**Mean SSIM Value**
653.68	0.76 ± 0.10
664.59	0.81 ± 0.07
675.51	0.86 ± 0.05
686.42	0.89 ± 0.04
697.33	0.91 ± 0.02
708.25	0.92 ± 0.01
719.16	0.93 ± 0.01
730.07	0.93 ± 0.01
740.99	0.93 ± 0.01
751.90	0.93 ± 0.01

Table 8. 3 bands selection with it correspondent SSIM values for Brain Cubes

5 Brain Histology Images	
Wavelength (nm)	**Mean SSIM Value**
686.42	0.89 ± 0.04
719.16	0.93 ± 0.01
751.90	0.93 ± 0.01

From the 10 and 3 bands selected, new cubes were generated. Furthermore, grayscale cubes were generated from the mean of the 10 and 3 bands, respectively. Table 9 presents the mean value of the SSIM for the aforementioned cubes using different configurations strategies for comparison purposes.

Table 9. Mean Values of SSIM for different Brain cube configurations

5 Brain Histology Images	
Configuration Name	**Mean SSIM Value**
Best single band (719.16 nm)	0.93 ± 0.01
10 selected bands	0.88 ± 0.04
10 selected bands grayscale	0.91 ± 0.03
3 selected bands	0.92 ± 0.01
3 selected bands grayscale	0.94 ± 0.01

As we can appreciate in Table 9, composite image is not much better than the best single band by its own. However, we must consider the application we are stitching these images for. In this Master Thesis, stitching is performed to generate macro images where histopathologists will be able to find anomalies for brain cancer detection. Moreover, machine learning algorithms may also use this type of images to automatically predict these anomalies. Thus, single band images are not interesting for these applications and composites of several bands should be made. Overall, the new cubes produce good mosaic results (SSIM > 0.85) and so, they could be used for the aforementioned applications. In Figure 34, we can observe the qualitative results for the mosaic of the best band (Figure 34.b), the 3-band cube (Figure 34.c) and the gray image extracted from the mean of the 3 selected bands (Figure 34.d), compared to the original RGB image (Figure 34.a). However, as the bands composing these mosaics are between 650 and 750 nm, all the structures present in original image are not present in the mosaics, as they were not at these wavelengths.

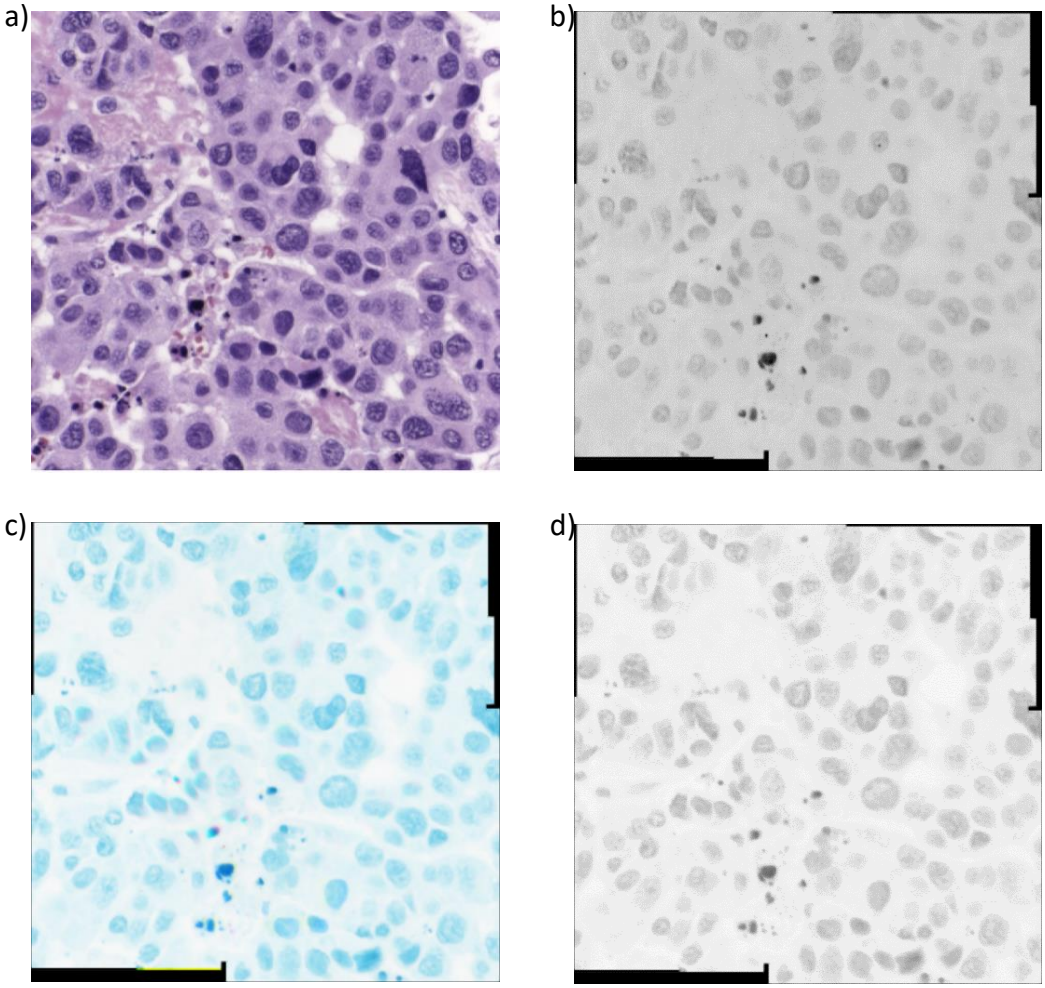

Figure 34. a) Original synthetic RGB brain histology image (275 bands), b) Mosaic of best single band (grayscale representation), c) Mosaic of 3 selected bands (false color image) and d) Mosaic of 3 selected bands grayscale.

Lastly, and as in the previous steps, the procedure was repeated with the breast cancer cubes. Same 10 and 3 bands were selected, and cubes made. Table 10, Table 11 and Table 12 show the corresponding results. Similarly, to the brain histology images, breast histology images results are not much better in one configuration than another. It is necessary to be able to form different channel cubes for the application we need the mosaics for, and in Table 12 it is shown that it is possible to do it obtaining good stitching results (SSIM > 0.93).

Table 10. 10 bands selection with it correspondent SSIM values for Breast Cubes

4 Breast Histology Images	
Wavelength (nm)	**Mean SSIM Value**
652.95	0.75 ± 0.04
663.86	0.82 ± 0.02
674.78	0.87 ± 0.01
685.69	0.91 ± 0.01
696.61	0.93 ± 0.00
707.52	0.94 ± 0.00
718.43	0.95 ± 0.00
729.35	0.95 ± 0.00
740.26	0.95 ± 0.00
751.17	0.91 ± 0.04

Table 11. 3 bands selection with it correspondent SSIM values for Breast Cubes

4 Breast Histology Images	
Wavelength (nm)	**Mean SSIM Value**
685.69	0.91 ± 0.01
718.43	0.95 ± 0.00
751.17	0.91 ± 0.04

Table 12. Mean Values of SSIM for different Breast cube configurations

4 Breast Histology Images	
Configuration Name	**Mean SSIM Value**
Best single band (718.43 nm)	0.95 ± 0.00
10 selected bands	0.93 ± 0.00
10 selected bands grayscale	0.95 ± 0.00
3 selected bands	0.94 ± 0.00
3 selected bands grayscale	0.93 ± 0.01

5.2.4. Manual vs Automatic Stitching

Next, a comparison between the different methods employed in this Master Thesis is presented. In Table 13 we show a summary of the results achieved with the manual and the automatic stitching methods, in yellow and green color columns respectively. To be able to do the comparison, the RGB of the manual algorithms was compared to the 3 selected bands from the automatic one. Same procedure was done for the 10 band images. For the gray image, in the manual stitching algorithm the mean of all the band was used, but for the automatic one, it was used the band which produced the most accurate result.

Table 13. Summary of main Results (Yellow is for manual and green for automatic stitching).

	Brain Histology Images					
	Manual RGB	**Automatic 3 Selected Bands**	**Manual 10 bands**	**Automatic 10 Selected Bands**	**Manual Grayscale**	**Automatic Best Single Band**
RMSE	0.10 ± 0.02	0.12 ± 0.00	0.08 ± 0.01	0.12 ± 0.01	0.07 ± 0.01	0.12 ± 0.00
PSNR (dB)	19.88 ± 1.70	18.63 ± 0.34	22.02 ± 0.89	18.25 ± 0.41	23.54 ±0.62	18.59 ± 0.17
SSIM	0.83 ± 0.03	0.92 ± 0.01	0.89 ± 0.02	0.88 ± 0.04	0.84 ± 0.04	0.93 ± 0.01

Results of Table 13 show that metrics are slightly better in green columns than in yellow ones. Furthermore, qualitative results show that the results of the automatic algorithm are better than the manual algorithms ones. Thus, we can conclude that Lang *et al.* [61] algorithm performs accurately when mosaicking hyperspectral histologic images.

In Figure 35 it is shown how these methods would behave in a real situation. Firstly, Figure 35.a and Figure 35.b show how is the original image, and how does it look when it is zoomed in. As taken at low magnification, spatial resolution is not the best. Moreover, Figure 35.c and Figure 35.d show how does it look a manually assembled mosaic. Single frames where taken at higher magnification and mosaicked one next to each other. The result is a high spatial resolution image, but bad alignment in the borders of the small frames because of the translational error produced by the platform. Finally, Figure 35.e and Figure 35.f show the result of an automatic stitching. Single frames were taken in the same way as the precious method, but assembled using the algorithm of Lang et al. [61] (3 frames at 67% overlap). The result is again a high spatial resolution image, but it does no reconstruct all the original image (just 83% of it) and we lose some quality at the borders of the mosaic. However, we consider that qualitatively the automatic method is better than the manual one since usually important features and characteristic which pathologist are looking for in a histology slide are located at the center of it. Thus, we are interested in a method that produces a good quality image in the center, and we are not much worried about the borders.

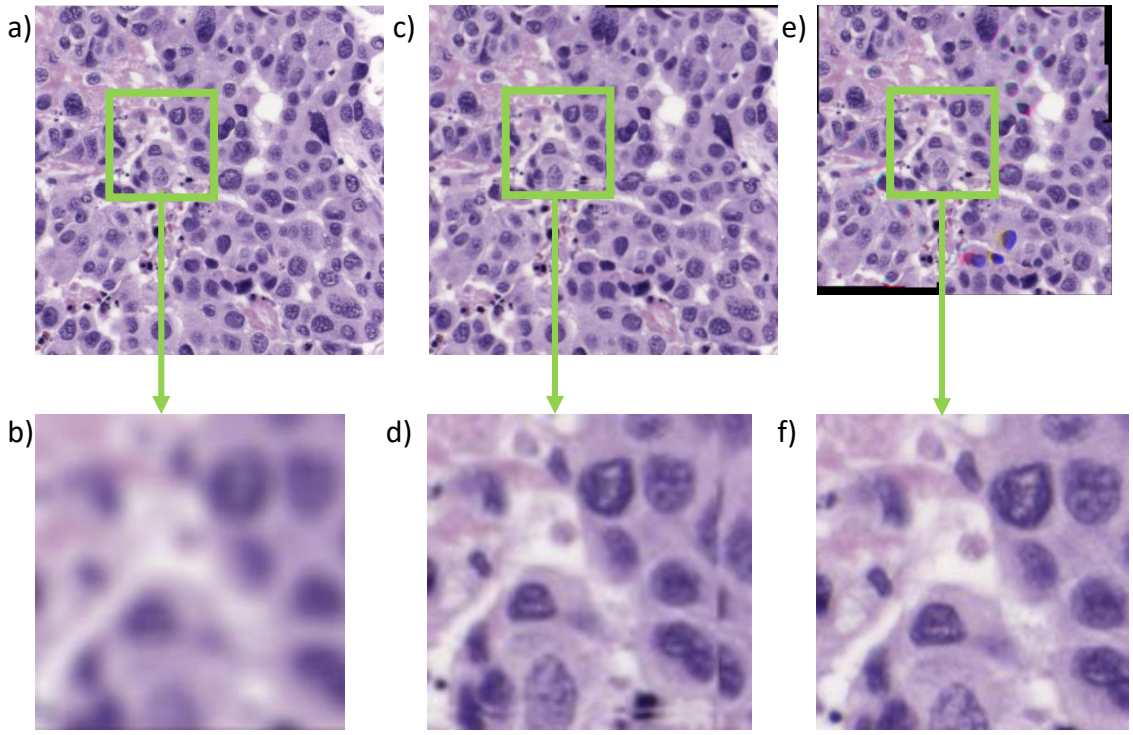

Figure 35. Simulation of a real situation. a) Original RGB image, b) Zoom of a produces a frame of low spatial resolution, c) Manual Stitched RGB Image, d) Zoom of c produces a frame of high spatial resolution but misalignments in the joints between frames, e) Automatic Stitched RGB Image, f) Zoom of e produces a frame of high spatial resolution but e image does not reconstruct the whole original image a.

5.3. Resources

In this last section, the resources employed in each test are shown and briefly commented. They were calculated using MATLAB R2019b in a Windows environment (Microsoft Windows 10) with an Intel i5-4210U 1.70 GHz CPU and 16 GB RAM. Time was obtained from the profile function, already incorporated in MATLAB. The output is displayed in seconds. The memory that each band need was measured using the function MONITOR_MEMORY_WHOS developed by Gardner, J. *et al.* [74], which uses the WHOS command and evaluates inside the BASE workspace and sums up the bytes. The output is displayed in MB. Once we had the time and memory that each frame consumes, we proceeded to calculate two mean values. On one hand, the mean of every configuration used in the frame and overlap selection, and, on the other hand, the mean of the values obtained in for every band in the band selection phase.

Table 14. Resource employed by the different tests

		Memory (MB)	Time (seconds)	Time (minutes)
Frames and overlap selection	**RGB**	2.49	331.87	5.52
	10 bands	6.83	816.18	13.60
	Grayscale	0.68	165.96	2.77
Band Selection		0.08	67.57	1.12

For the first step were the optimum overlap and frames were found, we can see some consistency since the 10 bands images spent more resources over the others, and so did the RGB images over the Grayscale ones. Furthermore, for the second step were the stitching algorithm was applied over every single band, we can see how the mean values of the resources were very low, since each single band did not have that much information.

Conclusions

In this chapter, the results obtained when applying the stitching to the HS histological images were shown and discussed. Firstly, the manual stitching images were shown to produce in general good quality mosaics, but presented bad alignment in the joint areas between frames. Then, it was found out that 3 frames gave the best metrics values and 67% overlap reproduced most of the original image for the frames selected. Afterwards, out of all the bands in the HS cube, the range 650-750 nm was shown to provide the best stitching results. Finally, several channel combinations were made as well as the resources cost of the different tests were briefly analyzed.

Chapter 6: Discussion and Conclusions

In the following section, the previously obtained results are discussed. This will lead us to conclude which is the minimum overlap and band methods necessary to achieve an accurate stitched image. Furthermore, the main limitations found during the experiments are described, as well as the future research lines for this project.

6.1. Fulfilled Objectives

The main goal of this master thesis was to apply stitching algorithms for automatic assembly of HS histological images. To this aim, the HS technology and its application in the medical field were exhaustive studied. Furthermore, the actual state-of-art algorithms currently used in the literature for image stitching was deeply studied. In this literature review, it was found that the number of studies applying stitching to HS images was very limited. Consequently, we hypothesized that an already existing image stitching algorithm, such as the one developed by Lang et al. [61], could be adapted to our type of data and its input image parameters further optimized.

In this work we proposed the use of two different type of stitching algorithms, manual and automatic. The first one, consisted in simply assembly the frames one next to each other, and the second one was designed by Lang *et al.* [61]. They presented a multichannel mosaicking algorithm which applies pairwise normalized cross-correlation as a basis for frame registration. They used sequential frames with large overlapping areas (94%) to produce the mosaic. Consequently, we hypothesized that smaller overlap region between frames could be used to still acquire an accurate stitched image. Furthermore, other variables such as the number of frames and the bands employed could improve the final assembly result.

A Wald Protocol was designed, where 20× brain histological images were firstly cut into pieces, introducing a small translational error similar to the one the microscope platform

would cause. Then, these small FOV frames were stitched (using both manual and automatic algorithms) together into a large FOV image. Finally, the mosaicked image would be compared against the original one in order to measure the quality of the image.

On one hand, the mosaics obtained from the manual stitching algorithm produced good metrics ($\mathrm{RMSE} = 0.10 \pm 0.02,\ \mathrm{PSNR} = 19.88 \pm 1.70, \text{and } \mathrm{SSIM} = 0.83 \pm 0.03$) because most of the image remains the same. However, qualitatively we can observe how the joints between images do not match, and since most of the time what is really interesting in a histological slide is located at the center of it, this method did not provide a valid solution.

On the other hand, the input images to the automatic algorithm developed by Lang *et al.* [61] were optimized. In the first step, all the overlaps from 50% to 92% with all their correspondent frames were tested for 5 brain histological images in the form of RGB, 10 bands and grayscale cubes. From the mean metric values results it was found that the optimal frames would be 3 and the overlap 67%. From these selected overlaps and frames, the stitched image reconstructs the 83% of the original image with good quality metrics ($\text{RGB images: } \mathrm{RMSE} = 0.13 \pm 0.01, \mathrm{PSNR} = 17.33 \pm 0.93, \mathrm{SSIM} = 0.78 \pm 0.05$). Additionally, when observing them qualitatively, they show to be a really accurate assembly of the original image.

Afterwards, single band stitching was performed. Charts representing metrics versus wavelength gave an idea of which channels performed better stitching for these kind of histology images. Specifically, the range of 650 to 750 nm gave the best results, having a maximum around the wavelength of 700 nm. Finally, several cubes assembly were performed. Two sets of 3 and 10 channels were chosen from the best performing channels, and new cubes were created. Grayscale images were also formed from the mean of each set independently. Thus, four image configuration were tested, being the 10-band image the worst one, followed by its grayscale image (mean of the 10 bands), the 3-band image and finally its grayscale one (mean of the 3 bands). This makes sense since the 10 bands were composed of worse wavelength performance than the 3 band selection cubes.

All the procedures were repeated for 4 breast histology images to prove the repeatability of the tests. Furthermore, the computational cost of each stitching approach was computed in order to be aware of the resources employed and take them into account for further acceleration and implementation into a whole slide image software.

6.2. Conclusions

Nowadays, the study of histology slides is regarded as the gold standard for the clinical diagnosis of cancer, and the trend is to digitalize histology slides for further automatic disease classification [16]. HSI is an emerging technology in the biomedical field which provides a large number of adjacent spectral bands allowing detection of materials in a scene with higher precision. Thus, the information provided by a HS image can be analyzed to detect, identify, or discriminate objects and patterns as well as the chemical composition of the material present at the scene [9].

However, spatial information provided by one HSI frame is usually low. Additionally, high magnification images are desired because of its high resolution but they have a lack of broad FOV. Microimage mosaicking enables stitching many small scenes together to aid visualization, quantitative interpretation, and mapping of microscale features, but achieving both microscopic resolution and macroscopic FOV optical imaging remains a central challenge in the field.

In this Master Thesis, it was studied the state-of-art referring the stitching algorithms of HS histology images. Experimental tests were performed, employing manual and automatic algorithms. Although, manual tests showed good results metrics, the joint between images were not as good. Lang *et al.* [61] algorithms proportioned good results when applying 3 frames to reconstruct the original image and a 67% of overlap between them. Single band stitching was also performed, finding a range of wavelength between 650 and 750 nm that provided accurate mosaics. Several combinations of bands within this range were tested and proved to be quantitative and qualitative good. According to our results, a single band image produced the best stitching result. However, since we need several wavelengths to be able to detect anomalies in the image, single band images are not the ideal for us. 3 and 10 band images gave also good results (SSIM > 0.85) and can be employed in the aforementioned application.

In conclusion, the main and partial objectives of these Master Thesis have been achieved. Although, a novel stitching algorithm have not been developed, several important findings have been made in order to create our own algorithm in a close future.

6.3. Limitations and Future Work

The main limitations that we can find in this work come from the actual nature of the algorithm. At the beginning of the project it was intended to develop our own stitching algorithm using registration images tools. However, obtained results were no satisfactory and we realized that its development was out of a Master Thesis timeframe. Thus, this project is based on an external algorithm where the majority of the parameters cannot be modified (such as the input of square images or the maximum number of HS bands

restricted to 10). This is the main reason for which it is proposed to develop our own algorithm in a future project. This new stitching algorithm will be based, as the Lang *et al.* [61] one, in frame registration. For each pair of frames assembly, frame registration will be made for all the bands of the histology cubes, and the registration providing the most accurate stitching would be applied to the rest of the channels. Thus, it is hypothesized, the more channels introduced into the algorithm the more likely it is to find the optimal alignment. Using such custom algorithm, we will be able of assembly HS cubes with a large number of channel, being able to use the resulting cube for creating HS cubes from an entire slide, which will can be subsequently used in tumor classification algorithms.

Bibliography

[1] M. L. Bondy *et al.*, “Brain tumor epidemiology: Consensus from the Brain Tumor Epidemiology Consortium,” *Cancer*, vol. 113, no. S7, pp. 1953–1968, Oct. 2008, doi: 10.1002/cncr.23741.

[2] D. N. Louis *et al.*, “The 2016 World Health Organization Classification of Tumors of the Central Nervous System: a summary,” *Acta Neuropathol.*, vol. 131, no. 6, pp. 803–820, Jun. 2016, doi: 10.1007/s00401-016-1545-1.

[3] G. A. Shaw and H. K. Burke, “Spectral Imaging for Remote Sensing,” *LINCOLN Lab. J.*, vol. 14, no. 1, 2003.

[4] S.-K. Lin, “Introduction to Remote Sensing. Fifth Edition.By James B. Campbell and Randolph H. Wynne, The GuilfordPress, 2011; 662 pages. Price: £80.75, ISBN 978-1-60918-176-5,” *Remote Sens.*, vol. 5, no. 1, pp. 282–283, Jan. 2013, doi: 10.3390/rs5010282.

[5] M. Halicek, H. Fabelo, S. Ortega, G. M. Callico, and B. Fei, “In-Vivo and Ex-Vivo Tissue Analysis through Hyperspectral Imaging Techniques: Revealing the Invisible Features of Cancer,” *Cancers (Basel).*, vol. 11, no. 6, p. 756, May 2019, doi: 10.3390/cancers11060756.

[6] M. Bacco *et al.*, “Smart farming: Opportunities, challenges and technology enablers,” in *2018 IoT Vertical and Topical Summit on Agriculture - Tuscany (IOT Tuscany)*, 2018, pp. 1–6, doi: 10.1109/IOT-TUSCANY.2018.8373043.

[7] “Proyecto ITHACA – Proyecto ACIISI 2018-19.” [Online]. Available: https://ithaca.iuma.ulpgc.es/. [Accessed: 06-Mar-2020].

[8] R. Szeliski, “Image alignment and stitching: A tutorial,” *Foundations and Trends in Computer Graphics and Vision*, vol. 2, no. 1. Now Publishers, Inc., pp. 1–10, 2006, doi: 10.1561/0600000009.

[9] H. Fabelo *et al.*, “HELICoiD project: a new use of hyperspectral imaging for brain cancer detection in real-time during neurosurgical operations,” in *Hyperspectral Imaging Sensors: Innovative Applications and Sensor Standards 2016*, 2016, vol. 9860, p. 986002, doi: 10.1117/12.2223075.

[10] P. Gustavo and A. Lara Rodríguez, “Técnicas de reconocimiento de imágenes para la

creación de fotomosaicos," Facultad de Ciencias y Humanidades de la Universidad del Valle de Guatemala, 2003.

[11] A. Camacho-Velasco, C. A. Vargas-García, F. A. Rojas-Morales, S. F. Castillo-Castelblanco, and H. Arguello-Fuentes, "Aplicaciones y retos del sensado remoto hiperespectral en la geología colombiana," *Rev. Fac. Ing.*, vol. 24, no. 40, p. 17, Sep. 2015, doi: 10.19053/01211129.3845.

[12] W. A. D. Anderson, *Pathology*, 6th Editio. Saint Louis, Mosby, 1971.

[13] J. S. Lowe and P. G. Anderson, "Histology," in *Stevens Lowes Human Histology*, Elsevier, 2015, pp. 1–10.

[14] C. Tilley, "Christopher D. M. Fletcher Diagnostic Histopathology of Tumors, 4th Edition Elsevier Saunders, Philadelphia, 2013. 2296 Pages. Price £313.95. ISBN-10: 1437715346; ISBN-13: 978-1437715347.," *Neuropathol. Appl. Neurobiol.*, vol. 41, no. 6, pp. 853–853, Oct. 2015, doi: 10.1111/nan.12210.

[15] S. Lang, M. Schmidt, C. Graef, and D. Gross, "Ein Karrierestart im „Dritten Reich"," *Pathologe*, vol. 40, no. 6, pp. 636–648, Nov. 2019, doi: 10.1007/s00292-019-0637-9.

[16] L. He, L. R. Long, S. Antani, and G. R. Thoma, "Histology image analysis for carcinoma detection and grading," *Comput. Methods Programs Biomed.*, vol. 107, no. 3, pp. 538–556, Sep. 2012, doi: 10.1016/j.cmpb.2011.12.007.

[17] S. Doyle, A. Madabhushi, M. Feldman, and J. Tomaszeweski, "A Boosting Cascade for Automated Detection of Prostate Cancer from Digitized Histology," 2006, pp. 504–511.

[18] S. Doyle, S. Agner, A. Madabhushi, M. Feldman, and J. Tomaszewski, "Automated grading of breast cancer histopathology using spectral clusteringwith textural and architectural image features," in *2008 5th IEEE International Symposium on Biomedical Imaging: From Nano to Macro*, 2008, pp. 496–499, doi: 10.1109/ISBI.2008.4541041.

[19] M. Guillaud *et al.*, "Subvisual chromatin changes in cervical epithelium measured by texture image analysis and correlated with HPV," *Gynecol. Oncol.*, vol. 99, no. 3, pp. S16–S23, Dec. 2005, doi: 10.1016/j.ygyno.2005.07.037.

[20] U. Jütting *et al.*, "Diagnosis and Prognosis of Neuroendocrine Tumours of the Lung by Means of High Resolution Image Analysis," *Anal. Cell. Pathol.*, vol. 18, no. 2, pp. 109–119, 1999, doi: 10.1155/1999/695907.

[21] J. Kong, H. Shimada, K. Boyer, J. Saltz, and M. Gurcan, "IMAGE ANALYSIS FOR AUTOMATED ASSESSMENT OF GRADE OF NEUROBLASTIC DIFFERENTIATION," in *2007 4th IEEE International Symposium on Biomedical Imaging: From Nano to Macro*, 2007, pp. 61–64, doi: 10.1109/ISBI.2007.356788.

[22] WHO, "Guide to cancer early diagnosis." p. 39, 2017.

[23] F. Y. Shan *et al.*, "Molecular Diagnostics and Pathology of Major Brain Tumors," in *Primary Intracranial Tumors*, IntechOpen, 2019.

[24] F. ELAmrawy, A. A. Othman, C. Adkins, A. Helmy, and M. I. Nounou, “Tailored nanocarriers and bioconjugates for combating glioblastoma and other brain tumors,” *J. Cancer Metastasis Treat.*, vol. 2, no. 3, p. 112, Mar. 2016, doi: 10.20517/2394-4722.2015.78.

[25] G. Lu and B. Fei, “Medical hyperspectral imaging: a review,” *J. Biomed. Opt.*, vol. 19, no. 1, p. 010901, Jan. 2014, doi: 10.1117/1.JBO.19.1.010901.

[26] H. Fabelo *et al.*, “HELICoiD project: a new use of hyperspectral imaging for brain cancer detection in real-time during neurosurgical operations,” 2016, p. 986002, doi: 10.1117/12.2223075.

[27] S. Ortega, H. Fabelo, R. Camacho, M. de la Luz Plaza, G. M. Callicó, and R. Sarmiento, “Detecting brain tumor in pathological slides using hyperspectral imaging,” *Biomed. Opt. Express*, vol. 9, no. 2, p. 818, Feb. 2018, doi: 10.1364/BOE.9.000818.

[28] A. Bjorgan, M. Denstedt, M. Milanič, L. A. Paluchowski, and L. L. Randeberg, “Vessel contrast enhancement in hyperspectral images,” 2015, p. 93180G, doi: 10.1117/12.2075703.

[29] H. Akbari, Y. Kosugi, K. Kojima, and N. Tanaka, “Detection and Analysis of the Intestinal Ischemia Using Visible and Invisible Hyperspectral Imaging,” *IEEE Trans. Biomed. Eng.*, vol. 57, no. 8, pp. 2011–2017, Aug. 2010, doi: 10.1109/TBME.2010.2049110.

[30] D. J. Mordant *et al.*, “Spectral imaging of the retina,” *Eye*, vol. 25, no. 3, pp. 309–320, Mar. 2011, doi: 10.1038/eye.2010.222.

[31] M. Milanic, A. Bjorgan, M. Larsson, T. Strömberg, and L. L. Randeberg, “Detection of hypercholesterolemia using hyperspectral imaging of human skin,” 2015, p. 95370C, doi: 10.1117/12.2183880.

[32] H. Ogihara, Y. Hamamoto, Y. Fujita, A. Goto, J. Nishikawa, and I. Sakaida, “Development of a Gastric Cancer Diagnostic Support System with a Pattern Recognition Method Using a Hyperspectral Camera,” *J. Sensors*, vol. 2016, pp. 1–6, 2016, doi: 10.1155/2016/1803501.

[33] S. Ortega, M. Halicek, H. Fabelo, G. M. Callico, and B. Fei, “Hyperspectral and multispectral imaging in digital and computational pathology: a systematic review [Invited],” *Biomed. Opt. Express*, vol. 11, no. 6, p. 3195, Jun. 2020, doi: 10.1364/BOE.386338.

[34] Q. Wang, J. Wang, M. Zhou, Q. Li, and Y. Wang, “Spectral-spatial feature-based neural network method for acute lymphoblastic leukemia cell identification via microscopic hyperspectral imaging technology,” *Biomed. Opt. Express*, vol. 8, no. 6, p. 3017, Jun. 2017, doi: 10.1364/BOE.8.003017.

[35] J. Lou, M. Zhou, Q. Li, C. Yuan, and H. Liu, “An automatic red blood cell counting method based on spectral images,” in *2016 9th International Congress on Image and Signal Processing, BioMedical Engineering and Informatics (CISP-BMEI)*, 2016, pp. 1391–1396, doi: 10.1109/CISP-BMEI.2016.7852934.

[36] Cheng Lu and M. Mandal, “Toward Automatic Mitotic Cell Detection and Segmentation in Multispectral Histopathological Images,” *IEEE J. Biomed. Heal. Informatics*, vol. 18, no. 2, pp. 594–605, Mar. 2014, doi: 10.1109/JBHI.2013.2277837.

[37] M. D. Zarella *et al.*, “A Practical Guide to Whole Slide Imaging: A White Paper From the Digital Pathology Association,” *Arch. Pathol. Lab. Med.*, vol. 143, no. 2, pp. 222–234, Feb. 2019, doi: 10.5858/arpa.2018-0343-RA.

[38] L. Pantanowitz, N. Farahani, and A. Parwani, “Whole slide imaging in pathology: advantages, limitations, and emerging perspectives,” *Pathol. Lab. Med. Int.*, p. 23, Jun. 2015, doi: 10.2147/PLMI.S59826.

[39] G. Bueno, O. Déniz, M. D. M. Fernández-Carrobles, N. Vállez, and J. Salido, “An automated system for whole microscopic image acquisition and analysis,” *Microsc. Res. Tech.*, vol. 77, no. 9, pp. 697–713, Sep. 2014, doi: 10.1002/jemt.22391.

[40] E. Romero, F. Gómez, and M. Iregui, “Virtual Microscopy in Medical Images: a Survey,” *Microsc. B. Ser. Mod. Res. Educ. Top. Microsc.*, vol. 571, pp. 996–1006, 2007.

[41] R. ALEXANDRE, “DEM Spatial Resolution - what does this mean for flood modellers? | JBA Risk Management,” 2018. [Online]. Available: https://www.jbarisk.com/news-blogs/dem-spatial-resolution-what-does-this-mean-for-flood-modellers/. [Accessed: 22-Mar-2020].

[42] W. Philips, S. Van Assche, D. De Rycke, and K. Denecker, “State-of-the-art techniques for lossless compression of 3D medical image sets,” *Comput. Med. Imaging Graph.*, vol. 25, no. 2, pp. 173–185, Mar. 2001, doi: 10.1016/S0895-6111(00)00046-X.

[43] J. R. Gilbertson, J. Ho, L. Anthony, D. M. Jukic, Y. Yagi, and A. V Parwani, “Primary histologic diagnosis using automated whole slide imaging: a validation study,” *BMC Clin. Pathol.*, vol. 6, no. 1, p. 4, Dec. 2006, doi: 10.1186/1472-6890-6-4.

[44] F. Yang, Z. S. Deng, and Q. H. Fan, “A method for fast automated microscope image stitching,” *Micron*, vol. 48, pp. 17–25, May 2013, doi: 10.1016/j.micron.2013.01.006.

[45] R. Szeliski, “Image Alignment and Stitching: A Tutorial,” *Found. Trends R Comput. Graph. Vis.*, vol. 2, no. 1, pp. 1–104, 2006, doi: 10.1561/0600000009.

[46] J. Chalfoun *et al.*, “MIST: Accurate and Scalable Microscopy Image Stitching Tool with Stage Modeling and Error Minimization,” *Sci. Rep.*, vol. 7, no. 1, pp. 1–10, Dec. 2017, doi: 10.1038/s41598-017-04567-y.

[47] Y. Y. Schechner and S. K. Nayar, “Generalized mosaicing: wide field of view multispectral imaging,” *IEEE Trans. Pattern Anal. Mach. Intell.*, vol. 24, no. 10, pp. 1334–1348, Oct. 2002, doi: 10.1109/TPAMI.2002.1039205.

[48] D. Capel and A. Zisserman, “Automated mosaicing with super-resolution zoom,” in *Proceedings. 1998 IEEE Computer Society Conference on Computer Vision and Pattern Recognition (Cat. No.98CB36231)*, pp. 885–891, doi: 10.1109/CVPR.1998.698709.

[49] P. Thévenaz and M. Unser, “User-friendly semiautomated assembly of accurate

image mosaics in microscopy," *Microsc. Res. Tech.*, vol. 70, no. 2, pp. 135–146, Feb. 2007, doi: 10.1002/jemt.20393.

[50] P. Viola and W. M. Wells, "Alignment by maximization of mutual information," in *Proceedings of IEEE International Conference on Computer Vision*, pp. 16–23, doi: 10.1109/ICCV.1995.466930.

[51] B. Appleton, A. P. Bradley, and M. Wildermoth, "Towards Optimal Image Stitching for Virtual Microscopy," in *Digital Image Computing: Techniques and Applications (DICTA'05)*, pp. 44–44, doi: 10.1109/DICTA.2005.79.

[52] M. Iregui, F. Gómez, and E. Romero, "Strategies for efficient virtual microscopy in pathological samples using JPEG2000," *Micron*, vol. 38, no. 7, pp. 700–713, Oct. 2007, doi: 10.1016/j.micron.2007.04.008.

[53] A. ROSENFELD and A. C. KAK, *Digital Picture Processing*. Elsevier, 1982.

[54] C. SUN, R. BEARE, V. HILSENSTEIN, and P. JACKWAY, "Mosaicing of microscope images with global geometric and radiometric corrections," *J. Microsc.*, vol. 224, no. 2, pp. 158–165, Nov. 2006, doi: 10.1111/j.1365-2818.2006.01687.x.

[55] C. Harris and M. A Stephens, "Combined corner and edge detector," in *Proceedings of the Fourth Alvey Vision Conference*, 1988, pp. 147–151.

[56] N. Bedard, T. Quang, K. Schmeler, R. Richards-Kortum, and T. S. Tkaczyk, "Real-time video mosaicing with a high-resolution microendoscope," *Biomed. Opt. Express*, vol. 3, no. 10, p. 2428, Oct. 2012, doi: 10.1364/BOE.3.002428.

[57] M. Guizar-Sicairos, S. T. Thurman, and J. R. Fienup, "Efficient subpixel image registration algorithms," *Opt. Lett.*, vol. 33, no. 2, p. 156, Jan. 2008, doi: 10.1364/OL.33.000156.

[58] D. E. Romo, J. Tarquino, J. D. García-Arteaga, and E. Romero, "Virtual slide mosaicing using feature descriptors and a registration consistency measure," 2013, p. 89220Q, doi: 10.1117/12.2035463.

[59] V. Rankov, R. J. Locke, R. J. Edens, P. R. Barber, and B. Vojnovic, "An Algorithm for image stitching and blending," 2005, p. 190, doi: 10.1117/12.590536.

[60] T. Vercauteren, A. Meining, F. Lacombe, and A. Perchant, "Real time autonomous video image registration for endomicroscopy: fighting the compromises," *Proc. SPIE - Int. Soc. Opt. Eng.*, vol. 6861, Feb. 2008, doi: 10.1117/12.763089.

[61] R. T. Lang, J. Tatz, E. M. Kercher, A. Palanisami, D. H. Brooks, and B. Q. Spring, "Multichannel correlation improves the noise tolerance of real-time hyperspectral microimage mosaicking," *J. Biomed. Opt.*, vol. 24, no. 12, p. 1, Dec. 2019, doi: 10.1117/1.JBO.24.12.126002.

[62] S. Ortega *et al.*, "Hyperspectral Imaging for the Detection of Glioblastoma Tumor Cells in H&E Slides Using Convolutional Neural Networks," *Sensors*, vol. 20, no. 7, p. 1911, Mar. 2020, doi: 10.3390/s20071911.

[63] S. Ortega *et al.*, "Hyperspectral Push-Broom Microscope Development and

Characterization," *IEEE Access*, vol. 7, pp. 122473–122491, 2019, doi: 10.1109/ACCESS.2019.2937729.

[64] L. Wald, T. Ranchin, and M. Mangolini, "Fusion of satellite images of different spatial resolutions: Assessing the quality of resulting images," *Photogramm. Eng. Remote Sens.*, vol. 63, no. 6, pp. 691–699, 1997.

[65] M. D. Zarella, M. R. Quaschnick;, D. E. Breen, and F. U. Garcia, "Estimation of Fine-Scale Histologic Features at Low Magnification," *Arch. Pathol. Lab. Med.*, vol. 142, no. 11, pp. 1394–1402, Nov. 2018, doi: 10.5858/arpa.2017-0380-OA.

[66] A. L. Bogdanov, J. Lapointe, and J. H. Schmid, "Electron-beam lithography for photonic waveguide fabrication: Measurement of the effect of field stitching errors on optical performance and evaluation of a new compensation method," *J. Vac. Sci. Technol. B, Nanotechnol. Microelectron. Mater. Process. Meas. Phenom.*, vol. 30, no. 3, p. 031606, May 2012, doi: 10.1116/1.3700439.

[67] L. Wei, Z. Zhong, C. Lang, and Z. Yi, "A survey on image and video stitching," *Virtual Real. Intell. Hardw.*, vol. 1, no. 1, pp. 55–83, Feb. 2019, doi: 10.3724/SP.J.2096-5796.2018.0008.

[68] P. Pradham, N. H. Younan, and R. L. King, "Concepts of image fusion in remote sensing applications," in *Image Fusion*, Elsevier, 2008, pp. 393–428.

[69] A. Hore and D. Ziou, "Image Quality Metrics: PSNR vs. SSIM," in *2010 20th International Conference on Pattern Recognition*, 2010, pp. 2366–2369, doi: 10.1109/ICPR.2010.579.

[70] Z. Wang, A. C. Bovik, H. R. Sheikh, and E. P. Simoncelli, "Image Quality Assessment: From Error Visibility to Structural Similarity," *IEEE Trans. Image Process.*, vol. 13, no. 4, pp. 600–612, Apr. 2004, doi: 10.1109/TIP.2003.819861.

[71] G. Wald, "The Receptors of Human Color Vision: Action spectra of three visual pigments in human cones account for normal color vision and color-blindness," *Science (80-.).*, vol. 145, no. 3636, pp. 1007–1016, Sep. 1964, doi: 10.1126/science.145.3636.1007.

[72] L. Giannoni, F. Lange, and I. Tachtsidis, "Hyperspectral imaging solutions for brain tissue metabolic and hemodynamic monitoring: past, current and future developments," *J. Opt.*, vol. 20, no. 4, p. 044009, Apr. 2018, doi: 10.1088/2040-8986/aab3a6.

[73] S. A. Robila, "Band reduction for hyperspectral imagery processing," *Proc. SPIE - Int. Soc. Opt. Eng.*, vol. 7533, Feb. 2010, doi: 10.1117/12.837953.

[74] Jacob R. Gardner *et al.*, "Deep Manifold Traversal: Changing Labels with Convolutional Features," St. Louis, 2015.